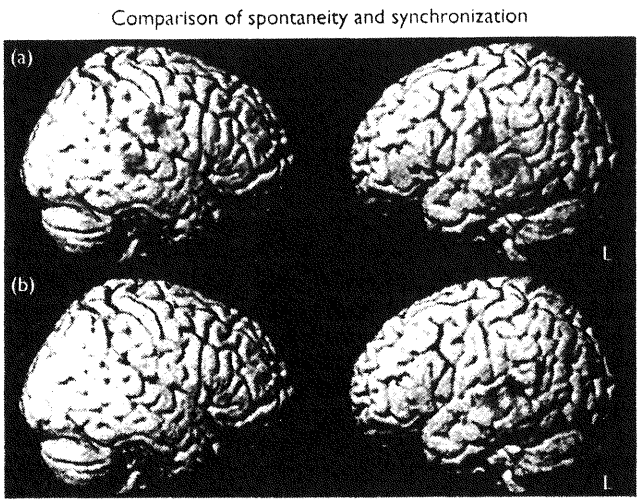

Fig. 1 Activations specific to the spontaneous process (green) and those specific to the synchronized process (red). (a) Singing; (b) speaking ($P < 0.05$, corrected).

the activation of the left anterolateral part of inferior frontal gyrus in singing is related not only to the spontaneous generation of text but also to that of melody [13]. Strong evidence indicates thats the major role played by the left inferior frontal gyrus is language generation in various aspects such as phonology, semantics, and syntax [18]. Damage to the left inferior frontal gyrus could cause a condition called dynamic aphasia, in which the patient faces a difficulty in producing spontaneous speech without any difficulty in naming, repetition, and comprehension. Robinson *et al.* [19] attributed this condition to the inability to select an appropriate verbal response from a large number of competing candidates. Warren *et al.* [20] reported the case of a patient suffering from dynamic aphasia owing to left inferior frontal gyrus atrophy who was able to generate melody without lyrics. Therefore, activity in the left inferior frontal gyrus may be related to the spontaneous generation of text rather than melody. Text generation in singing, however, is more complex than that in speaking, considering the need for supplying words for the tune and rhythm. This may explain the difference in the location of the left inferior frontal gyrus activation in singing and speaking. Another possible interpretation of the activation of left inferior frontal gyrus is associated with the increasing motor preparation [15] or cognitive control in spontaneous tasks.

On the other hand, activations specific for the spontaneous generation of melody, which imply the actions complementing the left inferior frontal gyrus activation, were not observed. The right inferior frontal gyrus and right anterior insula have been reported to be involved in melody generation [8,13]. In our study, these areas were found to be active specifically for singing but not for speaking under both spontaneous and synchronized conditions. These results suggest that the roles of the right inferior frontal gyrus and right anterior insula are not exclusive for the spontaneous condition. In addition, the right dorsal premotor cortex was observed as a singing-specific area regardless of spontaneous, synchronized, or listening conditions, implying that the right dorsal premotor cortex is involved in preparing the motor components of music production, such as melody and rhythm [6]. These findings suggest that melody and text generation in spontaneous singing of a well-learned song are not treated in parallel; melody might subsequently be generated along with text generation. To investigate the specific regions involved in the spontaneous generation of melody, the spontaneity and synchronization of pure melody, avoiding the influence of text, need to be examined in the future.

As the synchronized tasks relative to the spontaneous tasks contain two major components of external perception and synchronized production, activations to be detected by paired *t*-tests need to be interpreted in the light of the activation by passive listening tasks. Among the activations observed that are specific to the synchronized tasks, the posterior planum temporale was also activated by listening tasks. The left posterior planum temporale has been reported as common areas between covert singing and speaking and passive listening to songs and speech [14]. Moreover, the left posterior planum temporale has been reported to be involved in the processing and primary storage of various complex sound patterns [21]. Considering these points, the role of the left posterior planum temporale is not a passive perceptional function; it appears to play a more active role of bridging the external auditory information with further judgment and motor planning. The cortical region surrounding the left posterior Sylvian fissure in the posterior parietal–temporal boundary has been reported to be implicated in verbal working memory [22], auditory–motor integration for speech [23], and auditory–motor integration for both speech and music [24]. Our results suggest that the left posterior planum temporale plays an essential role in the synchronized processing of both melody and text, in combination with more specific regions: in combination with the bilateral anterior edge of the inferior parietal lobule and right posterior planum temporale, for synchronized singing, and with the left angular gyrus, for synchronized speaking. Activations in the left anterior edge of the inferior parietal lobule, right posterior planum temporale, right planum polare, and right middle insula were detected in synchronized singing as compared with synchronized speaking, suggesting that these areas are essential for processing melody rather than text under synchronized conditions [24,25].

Conclusion

Our results elucidate the neural networks of spontaneous and synchronized singing. The left inferior frontal gyrus may be essential for the spontaneous generation of text: the anterolateral part of the left inferior frontal gyrus in singing and pars triangularis of the left inferior frontal gyrus in speaking. In contrast, the right inferior frontal gyrus and right anterior insula are involved in melody generation regardless of spontaneous or synchronized conditions. On the other hand, the left posterior planum temporale plays the role of an auditory hub for synchronization of text and melody, in combination with the bilateral anterior edge of the inferior parietal lobule in singing and the left angular gyrus in speaking. Our findings suggest that text and melody in a well-learned song are not dealt with by symmetric or parallel networks. The neural mechanisms of spontaneous and synchronized singing will provide us with the basics to understand the neural mechanisms for a higher level of spontaneity (e.g. propositional speech and improvisation music), other forms of music (e.g. instrumental

melody and percussion), and their further application in education and rehabilitation.

Acknowledgement

We would like to thank Takashi Kodama, MSc, for the technical support.

References

1. Rao SM, Harrington DL, Haaland KY, Bobholz JA, Cox RW, Binder JR. Distributed neural systems underlying the timing of movements. *J Neurosci* 1997; **17**:5528–5535.
2. Jantzen KJ, Steinberg FL, Kelso JA. Brain networks underlying human timing behavior are influenced by prior context. *Proc Natl Acad Sci U S A* 2004; **101**:6815–6820.
3. Chen JL, Zatorre RJ, Penhune VB. Interactions between auditory and dorsal premotor cortex during synchronization to musical rhythms. *Neuroimage* 2006; **32**:1771–1781.
4. Gotell E, Brown S, Ekman SL. Influence of caregiver singing and background music on posture, movement, and sensory awareness in dementia care. *Int Psychogeriatr* 2003; **15**:411–430.
5. Perry DW, Zatorre RJ, Petrides M, Alivisatos B, Meyer E, Evans AC. Localization of cerebral activity during simple singing. *Neuroreport* 1999; **10**:3453–3458.
6. Langheim FJ, Callicott JH, Mattay VS, Duyn JH, Weinberger DR. Cortical systems associated with covert music rehearsal. *Neuroimage* 2002; **16**:901–908.
7. Riecker A, Ackermann H, Wildgruber D, Dogil G, Grodd W. Opposite hemispheric lateralization effects during speaking and singing at motor cortex, insula and cerebellum. *Neuroreport* 2000; **11**:1997–2000.
8. Jeffries KJ, Fritz JB, Braun AR. Words in melody: an $H_2{}^{15}O$ PET study of brain activation during singing and speaking. *Neuroreport* 2003; **14**: 749–754.
9. Peretz I, Kolinsky R, Tramo M, Labrecque R, Hublet C, Demeurisse G, Belleville S. Functional dissociations following bilateral lesions of auditory cortex. *Brain* 1994; **117**:1283–1301.
10. Hebert S, Racette A, Gagnon L, Peretz I. Revisiting the dissociation between singing and speaking in expressive aphasia. *Brain* 2003; **126**:1838–1850.
11. Serafine ML, Crowder RG, Repp BH. Integration of melody and text in memory for songs. *Cognition* 1984; **16**:285–303.
12. Koelsch S, Gunter TC, v Cramon DY, Zysset S, Lohmann G, Friederici AD. Bach speaks: a cortical 'language-network' serves the processing of music. *Neuroimage* 2002; **17**:956–966.
13. Brown S, Martinez MJ, Parsons LM. Music and language side by side in the brain: a PET study of the generation of melodies and sentences. *Eur J Neurosci* 2006; **23**:2791–2803.
14. Callan DE, Tsytsarev V, Hanakawa T, Callan AM, Katsuhara M, Fukuyama H, Turner R. Song and speech: brain regions involved with perception and covert production. *Neuroimage* 2006; **31**:1327–1342.
15. Ozdemir E, Norton A, Schlaug G. Shared and distinct neural correlates of singing and speaking. *Neuroimage* 2006; **33**:628–635.
16. Friston KJ, Holmes AP, Worsley KJ, Poline JB, Frith CD, Frackowiak RS. Statistical parametric mapping in functional imaging: a general linear approach. *Human Brain Mapp* 1995; **2**:189–210.
17. Makuuchi M, Kaminaga T, Sugishita M. Brain activation during ideomotor praxis: imitation and movements executed by verbal command. *J Neurol Neurosurg Psychiatry* 2005; **76**:25–33.
18. Vigneau M, Beaucousin V, Herve PY, Duffau H, Crivello F, Houde O, *et al.* Meta-analyzing left hemisphere language areas: phonology, semantics, and sentence processing. *Neuroimage* 2006; **30**:1414–1432.
19. Robinson G, Blair J, Cipolotti L. Dynamic aphasia: an inability to select between competing verbal responses? *Brain* 1998; **121**:77–89.
20. Warren JD, Warren JE, Fox NC, Warrington EK. Nothing to say, something to sing: primary progressive dynamic aphasia. *Neurocase* 2003; **9**:140–155.
21. Griffiths TD, Warren JD. The planum temporale as a computational hub. *Trends Neurosci* 2002; **25**:348–353.
22. Jonides J, Schumacher EH, Smith EE, Koeppe RA, Awh E, Reuter-Lorenz PA, *et al.* The role of parietal cortex in verbal working memory. *J Neurosci* 1998; **18**:5026–5034.
23. Wise RJ, Scott SK, Blank SC, Mummery CJ, Murphy K, Warburton EA. Separate neural subsystems within 'Wernicke's area'. *Brain* 2001; **124**: 83–95.
24. Hickok G, Buchsbaum B, Humphries C, Muftuler T. Auditory-motor interaction revealed by fMRI: speech, music, and working memory in area Spt. *J Cogn Neurosci* 2003; **15**:673–682.
25. Brown S, Martinez MJ, Hodges DA, Fox PT, Parsons LM. The song system of the human brain. *Cogn Brain Res* 2004; **20**:363–375.

ELSEVIER

NeuroImage

www.elsevier.com/locate/ynimg
NeuroImage 29 (2006) 1203 – 1211

MAP-based kinetic analysis for voxel-by-voxel compartment model estimation: Detailed imaging of the cerebral glucose metabolism using FDG

Yuichi Kimura,[a,*] Mika Naganawa,[c] Jun Yamaguchi,[b] Yuki Takabayashi,[b] Akihiko Uchiyama,[b] Keiichi Oda,[a] Kenji Ishii,[a] and Kiichi Ishiwata [a]

[a]*Positron Medical Center, Tokyo Metropolitan Institute of Gerontology, 1-1, Naka, Itabashi, Tokyo 173-0022, Japan*
[b]*Graduate School of Science and Engineering, Waseda University, 3-4-1, Ohkubo, Shinjyuku, Tokyo 169-8555, Japan*
[c]*Graduate School of Information Science, Nara Institute of Science and Technology, 8916-5, Takayama, Ikoma, Nara 630-0192, Japan*

Received 28 December 2004; revised 25 August 2005; accepted 31 August 2005
Available online 10 October 2005

We propose a novel algorithm for voxel-by-voxel compartment model analysis based on a maximum a posteriori (MAP) algorithm. Voxel-by-voxel compartment model analysis can derive functional images of living tissues, but it suffers from high noise statistics in voxel-based PET data and extended calculation times. We initially set up a feature space of the target radiopharmaceutical composed of a measured plasma time activity curve and a set of compartment model parameters, and measured the noise distribution of the PET data. The dynamic PET data were projected onto the feature space, and then clustered using the Mahalanobis distance. Our method was validated using simulation studies, and compared with ROI-based ordinary kinetic analysis for FDG. The parametric images exhibited an acceptable linear relation with the simulations and the ROI-based results, and the calculation time took about 10 min. We therefore concluded that our proposed MAP-based algorithm is practical.

Keywords: MAP; PET; Parametric image; FDG; Kinetic analysis

Introduction

The aim of this study was to develop a novel approach for voxel-by-voxel compartment model analysis to form parametric images using positron emission tomography (PET) based on a maximum a posteriori (MAP) approach.

PET can provide various functionalities of living tissues in the form of a spatial distribution of an administered radiopharmaceutical. If the details of a physiological function are required, then a history of the radiopharmaceutical concentrations in a tissue (i.e., the tissue time activity curve, or tTAC) is measured using multiple PET scans, and a compartment model analysis is applied to determine the parameters that describe the behavior of the administered drugs in a target organ (Huang and Phelps, 1986). This process is known as kinetic analysis. Furthermore, kinetic analysis in a voxel-by-voxel fashion provides us with images that can be used to determine the activity of specific enzymes or concentrations of neuroreceptors. However, voxel-based kinetic analysis has two major drawbacks. One is the noise level in a voxel-based tTAC, and the second is the large number of voxels involved. The noise level in a voxel-based tTAC leads to an instability in the estimated parameters. The large number of voxels, which can reach up to half a million, leads to extensive calculation times for image formation.

We have proposed a clustering-based algorithm to overcome this situation, in which voxel-based tTACs are categorized based on their kinetics. The algorithm, Clustering Analysis for Kinetics (CAKS), has been reported for a one-tissue-two-compartment model (Kimura et al., 1999), and a two-tissue-three-compartment model (Kimura et al., 2002). In the CAKS approach, the clustering algorithm is a key term. An unsupervised clustering scheme has also been applied (Kimura, 2004).

This paper introduces MAP approach for a kinetics scheme. This is proposed to improve a robustness for noise interference. In the proposed approach, feature surfaces are provided using an a priori knowledge of the kinetics of the administered radiopharmaceutical, and then, the observed data are clustered. Some simulation studies carried out are discussed to determine the details of the proposed algorithm, and to evaluate its reliability. Parametric images of the brain glucose metabolism are discussed using [^{18}F]fluoro-2-deoxy-D-glucose (FDG).

Method

In the proposed method, the estimated kinetic parameters of a voxel-based tTAC are determined based on similarities of shape, when data are compared with noise-free tTACs that are

* Corresponding author. Fax: +81 3 3964 2188.
E-mail address: ukimura@ieee.org (Y. Kimura).
Available online on ScienceDirect (www.sciencedirect.com).

1053-8119/$ - see front matter © 2005 Elsevier Inc. All rights reserved.
doi:10.1016/j.neuroimage.2005.08.046

formed from a set of parameters that lie within a physiologically feasible range. The shape of a noise-free tTAC is projected onto the feature space, and the noise is expressed as a statistical distribution of a feature point in the space.

Measurement of glucose metabolism using PET

FDG is a glucose analog, and it has been used to measure cerebral glucose metabolism using PET in glucose transport from plasma to tissue, in glucose phosphorylation, and to determine the metabolic rate of glucose.

The behavior of FDG is described by Eq. (1) (Huang et al., 1980):

$$C_o(t) = \frac{k_1}{\alpha_2 - \alpha_1}\{(k_3 + k_4 - \alpha_1)e^{-\alpha_1 t} + (\alpha_2 - k_3 - k_4)e^{-\alpha_2 t}\} \otimes C_p(t), \tag{1}$$

where

$$\alpha_1, \alpha_2 = \frac{k_2 + k_3 + k_4 \mp \sqrt{(k_2 + k_3 + k_4)^2 - 4k_2k_4}}{2}, \tag{2}$$

and $C_o(t)$ and $C_p(t)$ denote the concentration of administered FDG in a target tissue and arterial plasma, respectively. $\otimes$ denotes a convolution. Glucose transportation from a capillary to a tissue and the reverse process are described by the terms k_1 and k_2, respectively, and k_3 and k_4 denote the rate of phosphorylation and dephosphorylation of FDG. The term $C_o(t)$ is derived as a dynamic image from the PET data, and $C_p(t)$ is measured via arterial blood sampling. The term k_4 is ignored in our discussion, because we used scan durations of 60 min (Lucignani et al., 1993).

First, $C_o(t)$ was normalized using its integral to reduce the dimensionality by ignoring k_1, because k_1 appears in both the denominator and numerator of Eq. (3) from Eq. (1), and so cancels out.

$$C(t) = \frac{C_o(t)}{\int_0^{T_E} C_o(\tau)d\tau}, \tag{3}$$

where T_E denotes the time of the last frame.

Definition of the feature surface

The shape of $C(t)$ is represented mathematically as a surface in a feature space, in which a shape is represented by a position (Duda et al., 2001). To define a feature space, dynamic PET data are considered as a vector in n-dimensional space:

$$\boldsymbol{C} \equiv [C(t_1),..,C(t_n)]^T \tag{4}$$

where n is the number of frames. In a feature space, Cs are located at different points that have different shapes from each other.

In reality, the location of the noise-free tTACs in a feature space is identified before parameter estimation using the following steps. When the data from a measured plasma time activity curve (pTAC) are inputted into Eq. (1), a set of tTACs is derived by varying k_2 and k_3 in a suitable range based on physiological considerations: either 0.01 or values between 0.02 and 0.40 with a 0.02 step size for k_2, and values between 0.01 and 0.30 with a step size of 0.01 for k_3, where k_1 is fixed to 0.1. Then, all the generated tTACs are composed as a matrix C_A:

$$C_A \equiv [\boldsymbol{C}_1 ... \boldsymbol{C}_M], \tag{5}$$

and the principal components are calculated to generate a feature space.

If the noise-free tTACs are projected onto this space, shown as the C_1–C_4 in Fig. 1, a curved surface on the noise-free tTACs will be drawn, Π in Fig. 1. Note that first only some principal components are used. This approach decreases the dimensionality and simplifies further data analysis. The optimal dimensionality is discussed later in the text.

Parameter estimation

The noise distribution in a feature space, the likelihood for parameter estimation, is evaluated using the following procedure. To obtain the statistical properties of the noise in the measured tTACs, noisy tTACs are mimicked to add the simulated noise to the noise-free tTACs, assuming that a Gaussian distribution exists with a mean equal to that of the measured tTAC and a variance proportional to that of the tTAC (Kimura et al., 2002). This step means that a multidimensional Gaussian was assumed for the noise distribution in the projected tTAC onto the space. These values are used to determine the noise amplitude such that the simulated tTACs have the same noise level as those of the measured voxel-based tTACs.

The semantic diagram is available in Fig. 1. Noise-free tTACs are projected onto a point in the space defined by Eq. (4) (C_1–C_4 in Fig. 1). The noise perturbs the shape of the noise-free tTAC, and causes a fluctuation in the projected point. This fluctuation is assumed to be a multidimensional Gaussian, centered at its noise-free position of C_1–C_4. The covariances at each noise-free point are calculated using 500 realizations of noisy tTACs. To determine the associated cluster of the projected tTACs of A, the Mahalanobis distance between the point and each noise-free point is calculated, and then, the nearest point is selected. In our example, this is C_1. Finally, the

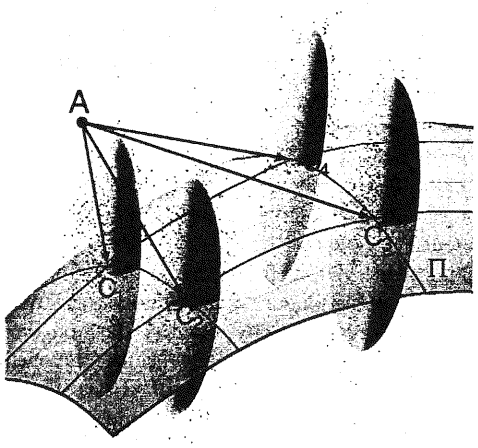

Fig. 1. A semantic diagram for parameter estimation using the proposed MAP-based algorithm. Π is a feature surface, and C_1–C_4 are the projected noise-free tTACs. Noisy projections are denoted by the smaller plots, and the estimated Gaussian is denoted by the superimposed ellipsoid. If a voxel-based tTAC is projected on A, then the Mahalanobis distance to each noise-free point can be calculated ($\overline{AC_1}$–$\overline{AC_4}$). Then, A can be classified as belonging to the nearest point of C_1.

corresponding values of k_2 and k_3 to the point are taken to be the estimates of the voxel-based tTAC. The ratio of the integral of the voxel-based tTAC to that of the corresponding noise-free tTAC determines the value of k_1.

Simulation

A simulation study was designed to determine the appropriate dimensionality of a feature space based on an estimation performance, and to validate the estimates using the proposed method. A clinically measured pTAC was applied to Eq. (1) with a set of k_1, k_2, and k_3 values varying from 0.01 to 0.19 with a step size of 0.02, from 0.01 to 0.28 with a step size of 0.03, and from 0.01 to 0.1 with a step size of 0.01, respectively. For each set of the parameters, 27 realizations of noise-free tTACs were generated, and Gaussian noise was added to simulate a real measurement situation. The proposed approach was applied, and the performance was evaluated to compare the data with the real values. Also, Patlak plot was employed to derive the estimates of k_1/k_2 (=DV) and the cerebral metabolic rate of glucose (CMRGlc) computed as:

$$\mathrm{CMRGlc} = \left(\frac{\mathrm{Gl}}{\mathrm{Lc}}\right) K_i \text{ where } K_i = \frac{k_1 k_3}{k_2 + k_3} \tag{6}$$

Gl is glucose content in blood, and Lc is a lamped constant of 0.42. In Patlak plot, the linear relation is established some minutes later after the administration:

$$\frac{C(t)}{C_\mathrm{p}(t)} = K_i \frac{\int_0^t C_\mathrm{p}(u)du}{C_\mathrm{p}(t)} + (\mathrm{DV} + \mathrm{Bv}) \tag{7}$$

where Bv denotes a blood volume. Therefore, the gradient and y-intercept gives us the estimates of CMRGlc and DV (Patlak et al., 1983).

Dimensionality

A dimensionality of feature space was decided using two ways: a performance-based approach as described in Simulation and a theoretical approach. Morgera (1985) proposed a covariance complexity based on an information theory, and it was calculated using the eigenvalues of an inputted data as defined in (Watanabe et al., 2003):

$$\sigma_j = \frac{\lambda_j^2}{\sum_{k=1}^{M} \lambda_k^2}, \tag{8}$$

$$\Gamma_M = -\frac{\sum_{j=1}^{M} \sigma_j \log \sigma_j}{\log M}, \tag{9}$$

where Γ_M denotes the complexity at the dimension of M, and λ_j is the jth eigenvalue of the covariance matrix of C_A sorted in descending order. Γ_M ranges on [0 1], and it represents a uniformity of information derived if M-dimensional feature space is employed. If all axes defining a feature space have almost the same amount of information, $\sigma_j \simeq 1 / M$, and Γ_M approaches to 1. Conversely, if only the first few axes have most information, the corresponding σ_js become almost 1, and $\Gamma_M \simeq 0$.

To investigate the dimensionality, voxel-based tTACs were generated the same as that described in Simulation with 500 realizations. k_1 was fixed at the typical value, and k_2 or k_3 varied in the range of their typical values ±50%. The values were 0.102, 0.130, and 0.062, respectively (Huang et al., 1980). Also, K_i varied in the range of 0.0334 ± 50% with the fixed k_1.

Clinical image

The proposed method was applied to clinical PET scans: five normal volunteers (four males and one female, average age = 22 ± 1.9), and two patients with congenital glucose transporter-1 deficiency (Pascual et al., 2002) (an 11- and a 7-year-old boy) to validate the algorithm in normal and higher than normal cases. The FDG doses injected were 233 ± 19 MBq for the normal subjects, and 155 or 121 MBq for the deficiency patients. The Ethics Committee of the Tokyo Metropolitan Institute of Gerontology approved the study protocol, and informed consent was given by all subjects. The scans were performed using a HEADTOME V apparatus (Shimadzu Corporation, Kyoto, Japan) with arterial blood sampling. The PET images were reconstructed at a resolution of 7.5 mm FWHM, with 128 × 128 voxels and 30 slices with 2 × 2 × 6.25 mm in a voxel size, using a standard convolution back-projection algorithm. Corrections were applied for dead time, detector nonuniformity, and for photon attenuation. The frame-time sequence was 10 s × 6, 30 s × 3, 60 s × 5, and 150 s × 5, and 300 s × 8. Besides, the images obtained from a 57-years-old female Alzheimer patient were formed using a HEADTOME-IV apparatus (Shimadzu Corporation, Kyoto, Japan) with 128 × 128 and 7 slices with 2 × 2 × 13 mm in a voxel size. The frame arrangements were 30 s × 2, 60 s × 4, 120 s × 4, 240 s × 8. The dose was 210 MBq. Parametric images of DV, CMRGlc were then computed. The delay between the tTAC and pTAC data was estimated using the tTAC averaged over all the regions of interest (ROIs) in a round-robin fashion (Kimura et al., 2004), and it was removed from voxel-based tTACs before applying the proposed method. Eq. (1) was fitted to the tTAC using the interior-reflective Newton method (Coleman and Branch,

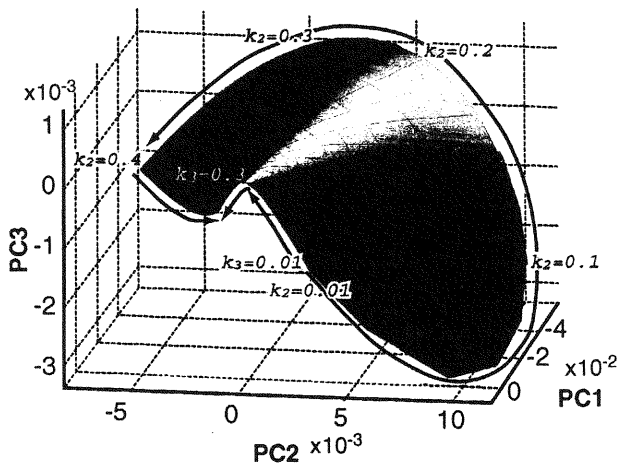

Fig. 2. Example of a feature surface generated in a three-dimensional space. Each axis denotes the first three principal components calculated from a given set of noise-free tTACs. Noise-free tTACs are projected onto this space and form a surface, as shown in the figure. The increase in the values of k_2 and k_3 is denoted by the black and gray arrows, respectively.

Fig. 3. An actual example of a feature surface and a projected tTACs. The projections are denoted by the small points. The surface is viewed from a low angle to emphasize its curled shape.

1999) with a nonnegative constraint. The initial estimates of all the parameters were selected to be 0.10. The blood volume was fixed at 0.03 (Martine et al., 1987). Before applying the proposed method to clinical data, blood volume component was also subtracted from voxel-based tTACs assuming the fixed blood volume. Additionally, extracranial voxels were manually excluded before the image formation.

To evaluate the consistency between the ordinary ROI-based model estimation and the estimates derived from the proposed algorithm, seven ROIs were selected: the frontal, occipital, parietal, temporal, cerebral, striatum, and the thalamus, and then the nonlinear estimation algorithm was applied to derive the estimates for the ordinary ROI-based kinetic analysis as described above.

Results

Feature surface

A typical feature surface is shown in Fig. 2, in which the generated tTACs are projected into three-dimensional space. It can be seen that the surface is highly curved as denoted by the black and gray arrows. The noise-free tTAC is represented by the lattice points on this surface, and the (k_2, k_3) parameter pair corresponds to one of these points.

Fig. 3 shows a real situation of feature points formed using measured PET data. The measured voxel-based tTACs are projected onto the feature surface denoted by the dots. The noise of the voxel-based tTAC fluctuated widely around the projected points. However, most of the points were located away from the surface because of the noise-induced fluctuation.

Simulation-based validation

Simulation-based validations are summarized in Fig. 4. For k_1, the estimated median values were almost identical to the true values. Moreover, there was an underestimation in this case, because the lower bars of the boxplots are longer than the upper bars. For k_3, the median value was almost the same as the true values, but the distribution of the estimates of k_3 was more complicated than that of k_1. In the case of smaller values of k_3, i.e., $k_3 < 0.03$, the estimate tends to be high. For values of k_3 larger than 0.08, the estimate was lower than the true value. For k_2, a linear

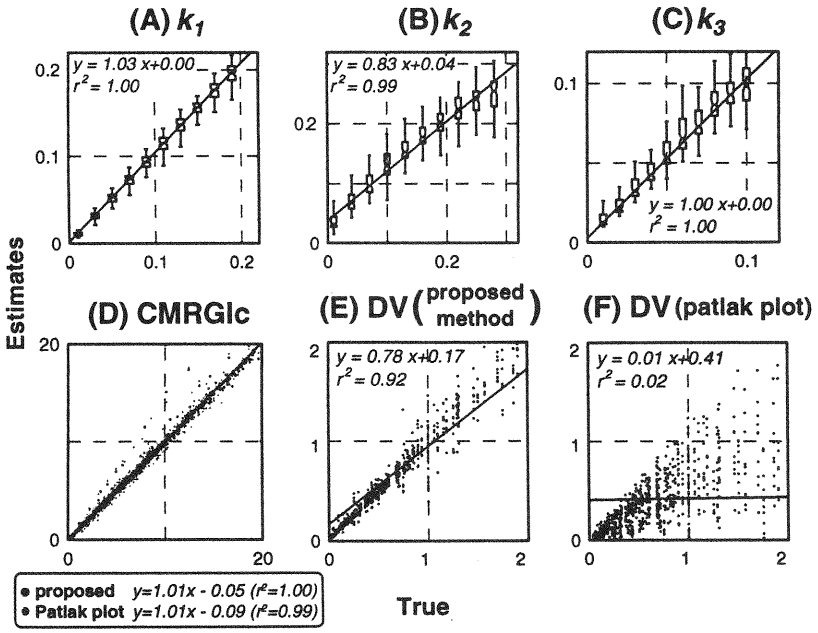

Fig. 4. Performance of the proposed algorithm in a simulation study. The estimates of k_1, k_2, and k_3 are plotted in panels A, B, and C, respectively. The estimates are plotted with respect to the true values as a boxplot. The lower, middle, and upper edges denote the 25th, 50th, and 75th percentiles, and the range shown between the lower and upper ticks is 1.5 times the quartile range, where most data exist. Regression lines between the true and the median are superimposed. CMRGlc estimated by the proposed algorithm and Patlak plot is plotted in panel D with black and gray points, respectively. And estimated DV using the proposed algorithm and Patlak plot is presented in panels E and F. For CMRGlc and DV, the estimates are plotted versus the true values. The regression lines are also shown.

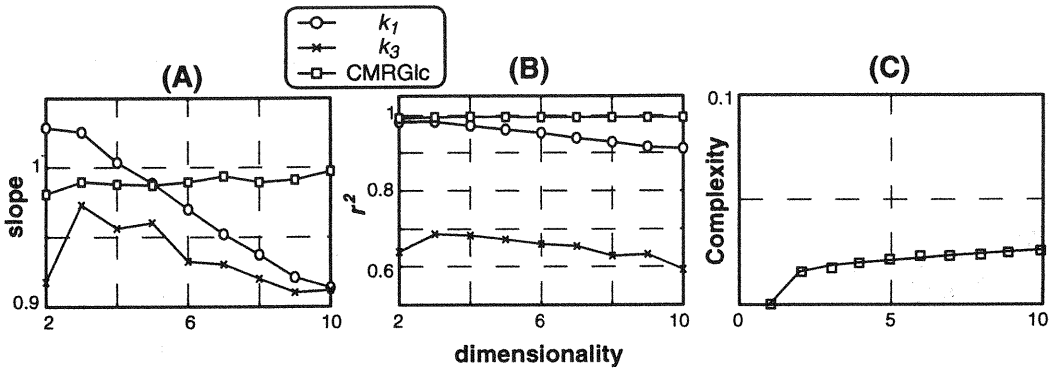

Fig. 5. Courses of a performance and complexity according to dimensionality. The performance comparisons according to the dimensionality of the feature space are shown in Frame (A), the change in consistency between the estimates and their true values, and in Frame (B), the change in linearity. For both quantities, the ideal values are 1. The typical change of covariance complexity is displayed in Frame (C).

relation was maintained, but it was 20% underestimated especially in large k_2 region. For CMRGlc shown in Fig. 4D, both estimates by Patlak plot and the proposed approach were almost identical with the true values, and the estimates from the proposed algorithm presented slightly better estimates. DV estimates showed different states between the proposed algorithm and Patlak plot in Figs. 4E and F. The proposed algorithm gave lineally correlated estimates, on the other hand in Patlak plot, no linear relation with the true DV could be found. The estimates using the proposed algorithm have 22% underestimation in the range of DV between 0 and 2.

Dimensionality

Performance comparisons against the dimensionality are shown in Figs. 5A and B. Frame (A) shows the change in slope of the regression lines between the estimates from the proposed algorithm derived for various dimensions and true values, where a slope equal to unity is the ideal case. For the CMRGlc data, there was no observed dependency on the dimensionality. For k_1, a higher dimensionality leads to an underestimation, and either two or three dimensions seem to be the optimum choice. For k_3, underestimation occurred with two dimensions or more than six dimensions. Frame (B) shows the calculated regression coefficients. The CMRGlc estimates always correlated well with the true values. The performance of the k_1 and k_3 estimates became gradually worse with increasing dimensionality. Three dimensions was the optimum choice based on the estimation performance.

The typical trend of covariance complexity is available in Frame (C) in cases of $k_1 = 0.102$, $k_2 = 0.13$, and $k_3 = 0.062$. Most information concentrated on the 1st dimension because the complexity was near its minimum of 0, and a large increase was observed only at the dimension of 2. And, further dimension in the feature space has approximately a uniform amount of information because the complexity gradually grew, but no peaks were observed according to the increase of dimensionality. These results implied that the information was not gained if higher dimensional feature space than 4 was utilized. This disposition was common in all k-parameters.

Clinical image

ROI-based validations are shown in Figs. 6 and 7, and typical clinical images are available in Fig. 8. For k_1, if it was smaller than 0.16 (which is normal range), the regression line was $y = 0.97x + 0.04$ ($r^2 = 0.90$); this line is plotted in a solid line in Fig. 6A, and both estimates were almost identical. However, the linear regression derived from all k_1 range was $y = 0.73x + 0.03$ ($r^2 = 0.96$), the dashed line in Fig. 6A, and 27% of underestimation was observed. For k_3 shown in Fig. 6C, if $k_3 < 0.13$ (the normal range of k_3), $y = 0.78x + 0.01$ ($r^2 = 0.92$), the solid line, and 22% of underestimation existed. The linear regression in all k_3 range was $y = 1.00x - 0.01$ ($r^2 = 0.91$); an almost identical relation. k_2 is summarized in Fig. 6B. The relation was $y = 0.57x + 0.12$ ($r^2 = 0.88$). For CMRGlc and DV, the comparisons between an ROI-based nonlinear estimation and the proposed algorithm or Patlak plot are illustrated in Fig. 7. Both CMRGlc estimates had good linear relations with 10% of underestimation as shown in CMRGlc-1 and CMRGlc-2; $y = 0.90x + 0.21$ ($r^2 = 0.98$) for the proposed algorithm and $y = 0.91x - 0.012$

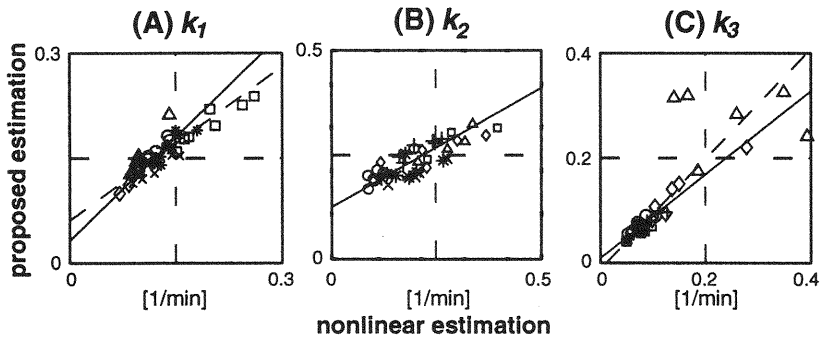

Fig. 6. Comparison between ordinary ROI-based nonlinear estimates and the proposed algorithm. Seven ROIs were placed on seven subjects, and subjects are plotted with different symbols. Regression lines derived from ordinary parameter range and from all estimates are plotted in solid and dashed lines, respectively.

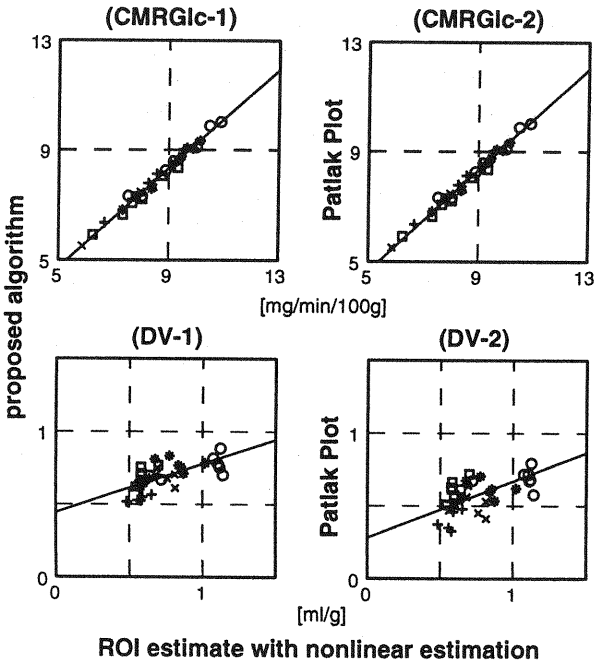

Fig. 7. Comparison between ordinary ROI-based nonlinear estimates and the proposed algorithm or Patlak plot on CMRGlc in (CMRGlc-1) and (CMRGlc-2), and on DV in (DV-1) and (DV-2). (CMRGlc-1) and (DV-1) were derived from the proposed algorithm, and (CMRGlc-2) and (DV-2) represent the estimates using Patlak plot. Seven ROIs were placed on seven subjects, and subjects are plotted with different symbols. Regression lines are superimposed.

($r^2 = 0.97$) for Patlak plot. The deviation of CMRGlc estimates with the proposed algorithm was 8% smaller than that with Patlak plot in the ROI-based validation. The relation of DV is not good; $y = 0.33x + 0.44$ ($r^2 = 0.96$) for the proposed algorithm and $y = 0.39x + 0.28$ ($r^2 = 0.97$) for Patlak plot in DV-1 and DV-2. The simulation showed that k_2 and DV had relatively poor linear relation and 20% of underestimation in Fig. 4, and the same results can be seen in the clinical results (Figs. 6B and 7DV-1). Also, the bias in DV estimates was not ignorable. Patlak plot can estimate DV, but it was poor as the proposed algorithm. The deviation of DV estimates by the proposed algorithm was around 35% smaller than those by Patlak plot in the ROI-based validation. However, in Fig. 8, the gray and white matter can be distinguished in the Alzheimer case, and also in the normal case because there was a monotonous relation between the DV estimates by the proposed algorithm and the ROI-based estimates. The performance of the proposed algorithm was rather sufficient for DV imaging. For CMRGlc, both estimates coincided well with each other. Generally, there is a good linear relation between both estimates in all parameters, and the CMRGlc and k_1 in its normal range were almost identical with the true values.

In the normal case in Fig. 8, the slices shown include the cerebellum and the thalamus. The brain structure is clearly visualized in the CMRGlc image, and in the k_1, k_3, and DV images. Some regional differences in glucose metabolism are observable: the cerebellum has a higher k_1 value than the cerebral cortex, and the k_3 value of the cerebellum is smaller than that in the cerebral cortex. In Alzheimer case, CMRGlc is clearly defected on the right temporal lobe. k_1, k_3, and DV are also lower than those in the left side. For CMRGlc, both methods give us a good brain structure, and the images with the proposed algorithm are less noisy than those with Patlak plot. For DV, the brain structure is unclear in the image with Patlak plot; however, the gray and white matter can be recognized in the proposed method.

It took about 10 min to generate a parametric image composed of 128 × 128 voxels and 30 slices using an Ultra-80 Workstation equipped with a 450 MHz Ultra SPARC-II processor and 4 gigabytes of memory (Sun Microsystems, Santa Clara, CA, USA), in which around 5 min was taken to generate the feature space and to calculate the covariances.

Discussion

We have discussed a novel scheme for voxel-based compartment model analysis methodology. Four points are covered in the discussion: the specificity of the algorithm to form a parametric image, a comparison with other methods for parametric imaging, the development of a MAP-based algorithm, and the performance and usability of the proposed approach.

We now discuss the difficulties encountered in parametric image formation using PET. PET can measure various functionalities in living tissues using a compartment model analysis. If the analysis is applied in a voxel-by-voxel fashion, then a functional image can be derived. Unfortunately, there are two serious drawbacks in voxel-based kinetic analysis. One is a high noise factor in voxel-based tTACs, and the other is the large calculation time required. The small volumes in voxels cause the high noise seen in voxel-based tTACs, and this leads to statistical uncertainties in the estimated kinetic parameters. If a nonlinear estimation algorithm is applied, then voxel-based parameter estimations tend to include large estimation variances and/or erroneous results because of this nonconvergence. Furthermore, a nonlinear estimation algorithm involves a considerable calculation time. The algorithm is usually implemented using an iterative approach, and typically, a compartment model analysis requires several dozen iterations. Additionally, a convolution operation is necessary to calculate a predicted output using a measured pTAC and interim parameters in these iterations, which is time-consuming. To make matters worse, the number of voxels can reach up to half a million. A PET camera has 128 × 128 voxels per slice, and can capture over 30 slices, giving a total of 5×10^5 voxels. For parametric image formation, the model estimation algorithm should be invoked at each voxel, so a huge calculation time is required. If it requires 10 s to obtain one voxel-based parameter estimation, then a couple of months will be required to form a parametric image. The above considerations make functional imaging in PET impractical.

The proposed approach is designed to overcome these problems using MAP algorithm. The model parameters are determined based on their proximity in the shape of a tTAC between a measured voxel-based tTAC and tTACs located in the bank of noise-free tTACs. The proposed approach tries to find most matched noise-free tTAC for a given feature space. Accordingly, the proposed approach does not invoke any parameter estimation algorithm, and the problems regarding parameter estimation and calculation time are therefore resolved.

The dimensionality of a feature space must be given a priori, because it defines the experimental space. In this study, an optimal

dimensionality was decided by using the simulation for validation method and a covariance complexity based on an information theory, as shown in Fig. 5. In the result, three dimensions were chosen as the optimum choice. The number of estimated parameters used was two: k_2 and k_3, because k_1 was ignored as shown in Eq. (3). This implies that a dimensionality higher than two is desirable to consider the noise in a tTAC. Moreover, the dimensionality must also be decided to take into account the signal-to-noise ratio. In Fig. 3, the projections were not located around the feature surface, but were widely scattered. This situation means that considerable noise was present. If the dimensionality used were too high, then a defined feature space would be composed of noise rather than the tTAC.

A covariance complexity denotes a uniformity of information in a given dimensionality and each axis defining a feature space. If the complexity is near 0, most information concentrates on first some axes. The result conveyed that the feature space was governed by the first some principal axes because the complexity was low; its maximum was 1.0 because of the definition, and it was smaller than 0.1 in all range of dimensionality. And, the complexity was increased at the dimension of two as shown in Fig. 5C, which represents that a new information can be expected if the 2nd axis is incorporated. In our performance-based simulation, at higher dimensions, the estimates were too low, and the linearity diminished. On balancing the number of parameters and quality of the input signal, three dimension remains the optimum choice. In the proposed algorithm, projected feature points are classified to multiple categories corresponding to pairs of k_2 and k_3 laid in a physiologically possible range. It is a complicated situation, and both information theory and performance-based indices are reasonable choices to decide the dimensionality for feature space definition.

We also compared the proposed method with other algorithms for voxel-based estimation. Some approaches linearize the compartment model to simplify the estimation process. Logan plot (Logan et al., 1996) and Patlak plot (Patlak et al., 1983) are popular algorithm choices for this operation, which uses a line estimation algorithm. RPM (Gunn et al., 1997) is another widely used algorithm used to visualize the binding potential using a spectrum approach. These algorithms are computationally simple and are therefore fast, because they are implemented with a linear estimation algorithm or a search for a minimal residual point from a table, and an iteration and convolution are not required. However, these algorithms can estimate only limited parameters: a distribution volume, an influx parameter, or a binding potential. Furthermore, the applicability of these algorithms depends on the

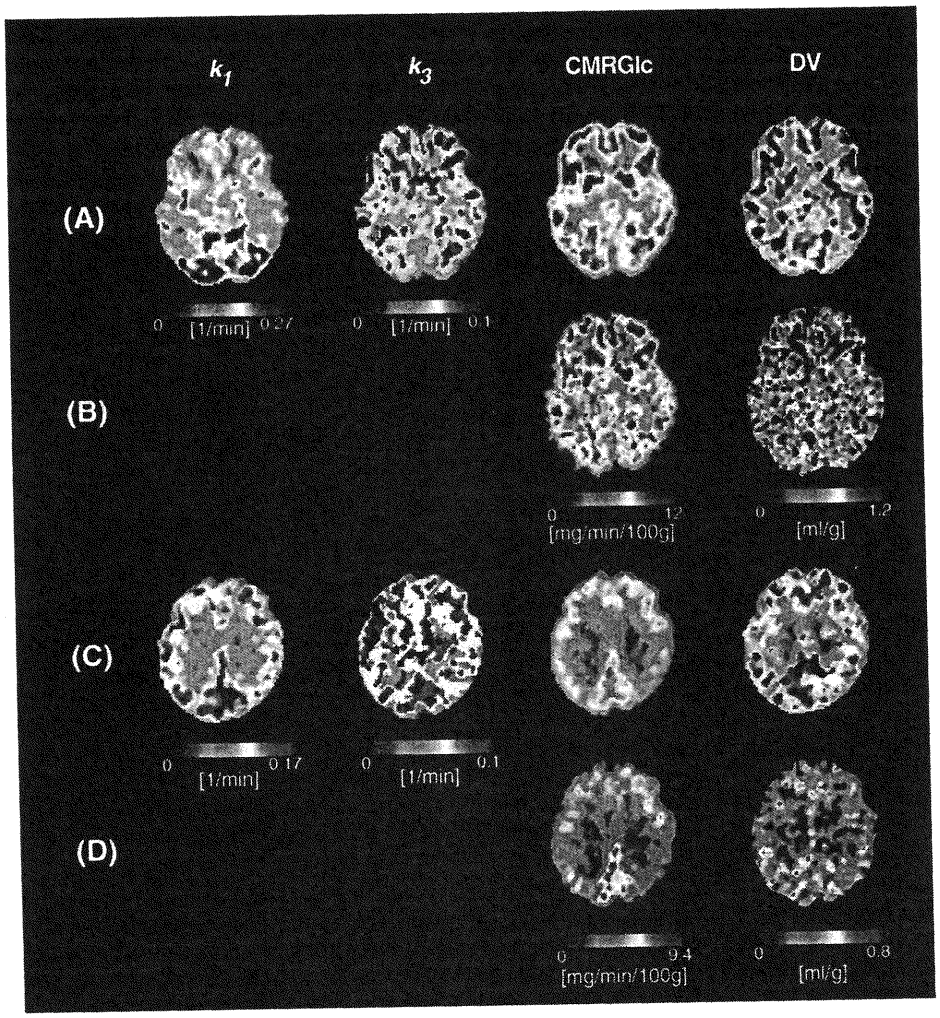

Fig. 8. Clinical images of glucose metabolism in a normal young female in panels A and B, and Alzheimer patient in panels C and D. Panels A and C were derived from the proposed algorithm, and panels B and D were formed by Patlak plot. All images were processed with a median filter.

kinetics of an administered radiopharmaceutical. Because FDG is trapped in a cell, then Logan plot and RPM are not applicable, but using Patlak plot is feasible. In contrast, the proposed algorithm can estimate all kinetic parameters, and is applicable to any compartment model, because the proposed approach is based on a general compartment model, and there is no assumption involved in the model kinetics. Likewise, for determination of optimal estimates, the method searches the nearest feature point instead of invoking nonlinear optimization algorithm which is usually utilized for a compartment model estimation. Accordingly, the proposed algorithm is computationally simple and fast.

We now consider the method based on statistical approach for medical image processing. An interesting study is the mixture analysis approach (O'Sullivan, 1993). O'Sullivan assumed tTACs as a weighted sum of sub-tTACs extracted from a dynamic data using a clustering algorithm. Clustering for PET data analysis was summarized in O'Sullivan (1994). Averaging dynamic data in voxels that belong to the same cluster improves the signal-to-noise ratio in voxel-based dynamic data, and it is helpful for parametric image formation (Kimura et al., 1999; Kimura et al., 2002; Kimura, 2004; Bentourkia, 2001; Wong et al., 2002; Bal et al., 2004; Guo et al., 2003). Additionally, it can reduce the number of data to be analyzed, and makes parametric image formation practical (Kimura et al., 1999; Kimura et al., 2002).

In Kimura (2004), an unsupervised clustering approach was implemented using a Gaussian mixture model. However, because of the large volume of data, the clustering algorithm used was rather unstable for convergence. In the proposed algorithm, MAP approach was introduced. The concept of MAP is that a priori knowledge is incorporated in order to develop the performance for parameter estimation. In MAP, an object function to be maximized for parameter estimation is composed as a sum of a likelihood and a priori probability (Sparacino et al., 2000). Various ways were proposed to define a priori knowledge: using maximum-likelihood estimates for the analysis of glucose contents in the blood (Sparacino et al., 2000), or using population-based values (Callegari et al., 2002), applying population-based averaged values to estimate FDG PET data (Bertoldo et al., 2004), including physiological constraints as a penalty term in an object function for model estimation (O'Sullivan and Saha, 1999) which can reduce estimation variance significantly for FDG imaging, and the approach was extended to spectral analysis (Trukheimer et al., 2003). In the method, a flat prior was defined in a parameter space which means that all parameters have even possibilities, and the Mahalanobis distance was introduced to realize MAP estimation using measured likelihoods derived from random sampling scheme.

The performance and usability of the proposed approach technique is now discussed. Both simulation and clinical studies showed that the estimates using the proposed algorithm approach were very close to, or had a linear relation to either the true parameters (Fig. 4) or to the ROI-based ordinary kinetic results (Figs. 6 and 7). The estimated CMRGlc data always coincided with both the true values and the ROI-based kinetic data, which are shown in Figs. 4D and Fig. 7 CMRGlc-1. In the CMRGlc image shown in Fig. 8, some cortical structures between the gray and white matter were well visualized, and the thalamus could be identified. For the k_1 data, the performance depended on the value used. In the range $k_1 < 0.16$ (the expected normal range of k_1), the estimate was almost identical, shown by the solid line in Fig. 6A. In addition, there was a 27% underestimation for larger k_1 values, shown by the dashed line in Fig. 6A. However, it can be said that the estimates are linearly correlated with the ROI-based kinetic results for all ranges of k_1. The performance of k_3 was worse than that of k_1. In the expected normal range of k_3, i.e., $k_3 < 0.13$, the estimate was 27% underestimated from the results of the ROI-based kinetic analysis. For higher values of k_3, the estimates had almost identical values with the ROI-kinetics. Moreover, for all ranges of k_3, a linear relation existed.

CMRGlc and DV were compared with Patlak plot in Figs. 4 and 7. Patlak plot is a well-established graphical approach which enables voxel-based calculation of both quantities. For CMRGlc, these two methods can offer good estimates and they were almost identical with an ordinal ROI-based kinetic analysis. While for DV, a situation was worse. The DV by the proposed algorithm was largely underestimated and only weak linear relation could be found. In clinical images of CMRGlc and DV in Fig. 8, the images derived from the proposed algorithm were less noisy than those made by Patlak plot especially in DV images; the estimation deviations derived from the proposed algorithm were 8% and 35% smaller than those of Patlak plot for CMRGlc and DV, respectively. Patlak plot calculates DV as a y-intercept, and it is sensitive for an estimation variance in a gradient of the plot. In the proposed approach, noise propagation in a voxel-based tTAC is considered as a likelihood function on the feature surface, and it might contribute an image quality developed.

Usually in FDG PET study, only CMRGlc is utilized for clinical purposes because a CMRGlc image contains some information for brain pathophysiology and it is easy to measure. Some previous works concluded that glucose transporters (Kalaria and Harik, 1989) and a clearance rate of glucose (Feinendegen et al., 2001) were affected by Alzheimer disease or cerebral infarction. Kalaria (Kalaria and Harik, 1989) reported that the hexose transporter located in the brain capillary was significantly decreased in Alzheimer patients. Also, k_1 images in Alzheimer patients have lower parts in the temporal lobe as shown in Fig. 8. They suggested that there is potential usefulness for the study of cerebral metabolism, and the method for voxel-by-voxel compartment model analysis should be developed. In the images in Fig. 8, the brain structure was well visualized, and a defect part in Alzheimer case is available. Fig. 8 showed that the glucose transportation was not homogeneous, and that it was higher in the cerebellum than in the cerebral images. Moreover, the images on cerebral glucose metabolism have different appearance between normal and Alzheimer case. This supports potential for more clinical application.

The overestimation and underestimation values speculated to originate from the distorted shape of the feature surface are shown in Fig. 2. The surface has a topologically quadrangular shape, but it is mostly curved. In the case of large k_3 values, the surface becomes narrow, and the projections of the measured voxel-based tTACs fluctuate in a wider range of parameter values than those of smaller k_3 values. This local difference in shape probably influences the different performances in the estimates. Furthermore, k_1 was a constant during generating noisy tTACs to calculate covariances on the feature surface, see Fig. 1, and a variance of tTAC was assumed to be proportional to the true tTAC value. The current algorithm ignores the dependency of noise distribution on an amplitude of tTAC. It would be needed to develop the algorithm in which tTAC amplitudes is considered. Using the proposed method, the noise propagation from the measured tTAC to the kinetic parameters was modeled in a statistical fashion, and it was

successful in realizing reliable estimates. More complicated statistical modeling is possible, but the proposed multivariate Gaussian scheme is a reasonable choice.

In summary, the proposed algorithm provides good CMRGlc images, which are identical to those from ordinary ROI-based kinetic analysis. The k_1 images are almost identical for values in the normal range. Images show underestimated k_3 and DV; however, the contrast is well maintained. The proposed scheme is theoretically expandable to the compartment model analysis for receptor kinetics because of no assumption for compartment model estimation. However, it causes an increase of the number of parameters, and the shape of feature surface becomes presumably more complex. More robust algorithm will be required.

Acknowledgment

This work was partially supported by the Japan Society for the Promotion of Science, Grant-in-Aid for Scientific Research (C), No. 16591243, 2004 and 2005.

References

Bal, H., DiBella, E.V.R., Gullberg, G.T., 2004. Parametric image formation using clustering for dynamic cardiac SPECT. IEEE Trans. Neural Netw. 50, 1584–1589.

Bentourkia, M., 2001. A flexible image segmentation prior to parametric estimation. Comput. Med. Imaging Graph. 25, 501–506.

Bertoldo, A., Spracino, G., Cobelli, C., 2004. Population approach improves parameter estimation of kinetic models from dynamic PET data. IEEE Trans. Med. Imag. 23, 297–306.

Callegari, T., Caumo, A., Cobelli, C., 2002. Generalization of map estimation in SAAM II: validation against ADAPT II in a glucose model case study. Ann. Biomed. Eng. 30, 961–968.

Coleman, T., Branch, M.A., 1999. Nonlinear least-squares. Optimization Toolbox User's Guide. MathWorks Inc., pp. 3–11 (Version 2).

Duda, R.O., Hart, P.E., Stork, D.G., 2001. Bayesian decision theory—Continuous features. Pattern Classification, (Second ed.)John Wiley and Sons, Inc., pp. 24–26.

Feinendegen, L.E., Herzog, H., Thompson, K.H., 2001. Cerebral glucose transport implies individualized glial cell function. J. Cereb. Blood Flow Metab. 21, 1160–1170.

Gunn, R.N., Lammertsma, A.A., Hume, S.P., Cunningham, V.J., 1997. Parametric imaging of ligand–receptor binding in PET using a simplified reference region model. NeuroImage 6, 279–287.

Guo, H., Renaut, R., Chen, K., Reiman, E., 2003. Clustering huge data sets for parametric PET imaging. Biosystems 71, 81–92.

Huang, S.C., Phelps, M.E., 1986. Principles of tracer kinetic modeling in positron emission tomography and autoradiography. In: Phelps, M.E., Mazziotta, J.C., Schlbert, H.R. (Eds.), Positron Emission Tomography and Autoradiography—Principles and Applications for the Brain and Heart. Raven Press, New York, USA, pp. 287–346.

Huang, S.C., Phelps, M.E., Hoffman, E.J., Sideris, K., Selin, C.J., Kuhl, D.E., 1980. Noninvasive determination of local cerebral metabolic rate of glucose in man. Am. J. Physiol. 238, E69–E82.

Kalaria, R.N., Harik, S.I., 1989. Reduced glucose transporter at the blood–brain barrier and in cerebral cortex in Alzheimer disease. J. Neurochem. 53, 1083–1088.

Kimura, Y., 2004. Formation of parametric image with statistical clustering. In: Iida, H., Shah, N.J., Hayashi, H., Watabe, H. (Eds.), Quantitation in Biomedical Imaging with PET and MRI, International Congress Series, vol. 1265. Elsevier, pp. 25–30.

Kimura, Y., Hsu, H., Toyama, H., Senda, M., Alpert, N.M., 1999. Improved signal-to-noise ratio in parametric images by cluster analysis. NeuroImage 9, 554–561.

Kimura, Y., Senda, M., Alpert, N.M., 2002. Fast formation of statistically reliable FDG parametric images based on clustering and principal component. Phys. Med. Biol. 47, 455–468.

Kimura, Y., Ishii, K., Fukumitsu, N., Oda, K., Sasaki, T., Kawamura, K., Ishiwata, K., 2004. Quantitative analysis of adenosine A_1 receptors in human brain using positron emission tomography and [1-methyl-^{11}C]8-dicyclopropylmethyl-1-methyl-3-propylxanthine. Nucl. Med. Biol. 31, 975–981.

Logan, J., Fowler, J.S., Volkow, N.D., Wang, G.J., Ding, Y.S., Alexoff, D.L., 1996. Distribution volume ratios without blood sampling from graphical analysis of PET data. J. Cereb. Blood Flow Metab. 16, 834–840.

Lucignani, G., Schmidt, K.C., Moresco, R.M., Striano, G., Colombo, F., Sokoloff, L., Fazio, F., 1993. Measurement of regional cerebral glucose utilization with Fluorine-18-FDG and PET in heterogeneous tissues: theoretical considerations and practical procedure. J. Nucl. Med. 34, 360–369.

Martine, W.R.W., Powers, W.J., Raichle, M.E., 1987. Cerebral blood volume measured with inhaled C^{15}O and positron emission tomography. J. Cereb. Blood Flow Metab. 7, 421–426.

Morgera, S.D., 1985. Information theoretic covariance complexity and its relation to pattern recognition. IEEE Trans. Syst. Man Cybern. SMC-15, 608–619.

O'Sullivan, F., 1993. Imaging radiotracer model parameters in PET: a mixture analysis approach. IEEE Trans. Med. Imag. 12, 399–412.

O'Sullivan, F., 1994. Metabolite images from dynamic positron emission tomography studies. Stat. Methods Med. Res. 3, 87–101.

O'Sullivan, F., Saha, A., 1999. Use of ridge regression for improved estimation of kinetic constants from PET data. IEEE Trans. Med. Imag. 18, 115–125.

Pascual, J.M., van Heerrtum, R.L., Wang, D., Engelstad, K., Vivo, D.C.D., 2002. Imaging the metabolic footprint of Glut1 deficiency on the brain. Ann. Neurol. 52, 458–464.

Patlak, C.S., Blasberg, R.G., Fenstermacher, J.D., 1983. Graphical evaluation of blood-to-brain transfer constants from multiple-time uptake data. J. Cereb. Blood Flow Metab. 3, 1–7.

Sparacino, G., Tombolato, C., Cobelli, C., 2000. Maximum-likelihood versus maximum *a posteriori* parameter estimation of physiological system models: the C-peptide impulse response case study. IEEE Trans. Biomed. Eng. 47, 801–811.

Trukheimer, F.E., Hinz, R., Gunn, R., Aston, J.A.D., Steve, R., Gunn, V.J.C., 2003. Rank-shaping regularization of exponential spectral analysis for application to functional parametric mapping. Phys. Med. Biol. 48, 3819–3841.

Watanabe, T.A.A., Cellucci, C.J., Kohegyi, E., Bashore, T.R., Josiassen, R.C., Greenbaun, N.N., Rapp, P.E., 2003. The algorithmic complexity of muitichannel EEGs is sensitize to change in behavior. Psychophysiology 40, 77–97.

Wong, K.P., Feng, D., Meikle, R., Fulham, M.J., 2002. Segmentation of dynamic PET images using cluster analysis. IEEE Trans. Med. Imag. 49, 200–207.

Journal of Cerebral Blood Flow & Metabolism (2006) 26, 291–300

www.jcbfm.com

Quantitative evaluation of cerebral hemodynamics in patients with moyamoya disease by dynamic susceptibility contrast magnetic resonance imaging—comparison with positron emission tomography

Yoji Tanaka[1], Tadashi Nariai[1], Tsukasa Nagaoka[1,2], Hideaki Akimoto[1,3], Kiichi Ishiwata[4], Kenji Ishii[4], Yoshiharu Matsushima[1] and Kikuo Ohno[1]

[1]*Department of Neurosurgery, Graduate School, Tokyo Medical and Dental University, Tokyo, Japan;* [2]*Department of Physiology and Biophysics, Albert Einstein College of Medicine, New York, New York, USA;* [3]*Department of Neurosurgery, Musashino Red Cross Hospital, Musashino, Japan;* [4]*Positron Medical Center, Tokyo Metropolitan Institute of Gerontology, Tokyo, Japan*

We examined whether the degree of hemodynamic stress in patients with chronic occlusive cerebral vascular disease can be quantitatively evaluated with the use of perfusion-weighted magnetic resonance imaging (PWI). Thirty-six patients with moyamoya disease (mean age, 26.8 years; range, 18 to 59) underwent PWI and positron emission tomography (PET) within a month's interval. The PWI data were calculated by three different analytic methods. The cerebral blood flow (CBF) ratio, cerebral blood volume (CBV) ratio, and mean transit time (MTT) of the anterior circulation were calculated using the cerebellum as a control region and compared with PET data on the same three parameters and oxygen extraction fraction (OEF). Parametric maps of PWI attained a higher resolution than the PET maps and revealed focal perfusion failure on a gyrus-by-gyrus level. The relative CBV and MTT obtained with PWI showed significant linear correlations with the corresponding PET values (CBV, $R^2 = 0.47$ to 0.58; MTT, $R^2 = 0.32$ to 0.68). We also found that we could detect regions with abnormally elevated OEF and CBV based on the delay of PWI-measured MTT relative to the control region by defining a 2.0-sec delay as a threshold. The sensitivity and specificity were 92.3% and 100% in detecting regions with abnormally elevated OEF, and 20.0% and 100% in detecting regions with abnormally elevated CBV, respectively. Among the parameters obtained with PWI, our results suggested that the relative CBV value and delay of MTT might be quantitatively manipulated to assist in clinical decision-making for patients with moyamoya disease.

Journal of Cerebral Blood Flow & Metabolism (2006) **26,** 291–300. doi:10.1038/sj.jcbfm.9600187; published online 27 July 2005

Keywords: blood volume; cerebral blood flow; misery perfusion; oxygen extraction fraction; transit time

Introduction

To understand the pathophysiology and determine the optimal treatment of occlusive cerebrovascular disease, it is vital to clarify the degree of hemodynamic compromise in each patient. Patients at a high risk of ischemic stroke generally exhibit abnormally high oxygen extraction fraction (OEF) and elevated cerebral blood volume (CBV), a combination of states described as misery perfusion or grade 2 hemodynamic stress (Derdeyn *et al,* 2002; Grubb *et al,* 1998). The concurrent measurement of cerebral blood flow (CBF), metabolism, and blood volume on the same occasion by positron emission tomography (PET) serves as the optimal method for evaluating hemodynamics in patients. Positron emission tomography is usually unavailable in daily clinical practice, however, and it provides only poor information on the structural integrity of hypoperfused tissue.

Perfusion-weighted magnetic resonance (MR) imaging (MRI) (PWI) provides various parameters

Correspondence: Dr Tadashi Nariai, Department of Neurosurgery, Tokyo Medical and Dental University, 1-5-45 Yushima, Bunkyo-ku, Tokyo 113, Japan. E-mail: nariai.nsrg@tmd.ac.jp
Received 1 February 2005; revised 13 May 2005; accepted 21 June 2005; published online 27 July 2005

of cerebral dynamics noninvasively and in less time than PET. A newly developed technique for determining absolute CBF using MRI by introducing an empirical normalization constant in animals (Ostergaard *et al,* 1998*b*) and humans (Ostergaard *et al,* 1998*a*) has recently been applied to evaluate occlusive cerebrovascular disorder (Baird and Warach, 1998; Maeda *et al,* 1999; Warach *et al,* 1996). To apply this technique effectively in decision-making for individual patients, however, we first have to clarify the reliability of the obtained parameters. In this study, we examined the same individual patients by PWI and PET within a short period in an attempt to confirm whether the numerical parameters obtained with PWI can be manipulated as quantitative values.

Moyamoya disease is a slowly progressive cerebrovascular disease with terminal internal carotid artery (ICA) occlusion and collateral formation of abnormal arteries (Matsushima, 1999; Suzuki and Takaku, 1969). Patients with moyamoya disease show various degrees of hemodynamic insufficiency and clinical symptoms. This variability might be due to the variable interaction between the worsening hemodynamic factors with disease progression and the protection conferred by the collateral development (Ikezaki *et al,* 1994; Nariai *et al,* 2005). The ischemic episodes in moyamoya patients are often caused by hemodynamic stress rather than thromboembolism (Ikezaki *et al,* 1994). These features of moyamoya disease make it an appropriate subject for comparing quantified hemodynamic factors with multiple modalities (Nariai *et al,* 1995). The use of PWI in moyamoya patients has been reported by several groups (Calamante *et al,* 2001; Kassner *et al,* 2003; Lee *et al,* 2003; Tsuchiya *et al,* 1998; Yamada *et al,* 1999). However, the accuracy of quantitative evaluation of cerebral hemodynamics by PWI in moyamoya patients has not yet been discussed. Moreover, we have yet to understand the significance of the abnormalities in the PWI parameters in relation to the severity of hemodynamics in patients with occlusive cerebrovascular disease. The purposes of the present study were to evaluate whether PWI can accurately measure hemodynamic parameters, and to certify the reliability of quantitation. We also discussed the range of application of this method in various types of cerebrovascular disease.

Subjects and methods

Forty-one examinations of 36 patients with angiographically confirmed moyamoya disease were evaluated in this study. The subjects consisted of 4 men and 32 women, ranging in age from 18 to 59 years (mean age, 26.8 years). All of the patients exhibited complete obstruction or stenosis in the terminal portion of bilateral ICA with moyamoya vessels, but no abnormal findings in cerebellar circulation. They underwent both PWI scan and PET scan within the same 30-day period for diagnosis or follow-up evaluation of cerebral hemodynamics. Five of the patients underwent postoperative scans at least 1 year after the bilateral indirect bypass surgery (encephalo-duro-arterio-synangiosis). The transient ischemic symptoms disappeared and good revascularization was confirmed by angiography in all five of these patients at the time of the scanning. Thus, their hemodynamic status was confirmed to be stable when the comparative examinations using PWI and PET were performed.

Perfusion-Weighted Magnetic Resonance Imaging

The MR imaging studies were performed using a 1.5-T superconducting system with a 25 mT/m maximal gradient capacity (Magnetom Vision; Siemens, Erlangen, Germany) and a circularly polarized head coil. Perfusion-weighted magnetic resonance imaging was performed using a multislice, single-shot, spin-echo echo-planar imaging sequence. The imaging parameters were as follows: repetition time = 1200 ms, echo time = 66 ms, field of view = $230 \times 230\,mm^2$, matrix size = 128×128. A total of 50 scans with 7 slices were repeated in quick succession without delay (3 scans before injection). The device scanned a series of seven 5-mm-thick slices separated by 7.5-mm gaps. The lowermost slice included the cerebellar hemisphere as a control area, and another slice included the ICA to enable estimation of the arterial input function (AIF). The seven slices were also set to cover both cerebral hemispheres. Each patient received a bolus injection of gadodiamide (0.2 mmol/kg body weight; OMNISCAN, Daiichi Seiyaku, Tokyo, Japan) via an antecubital vein using a power injector (Nemoto Kyorindo, Japan) at a rate of 3 mL/sec, followed by a 15-mL saline flush.

Perfusion-Weighted Magnetic Resonance Imaging Image Processing

All of the PWI data and PET data were transferred to a personal computer after the measurement. The PWI data were analyzed by three separate analyses using Dr View/LINUX R2.0 software (Asahi Kasei Information Systems, Tokyo, Japan). In preparation, we calculated the transverse relaxation rate (ΔR_2) by the equation $\Delta R_2(t) = -\ln(S(t)/S0)/TE$, where $S(t)$ was signal intensity at time t, $S0$ was the precontrast baseline signal intensity, and TE was the sequence echo time. Next, we applied a 3×3 uniform smoothing kernel to the raw image and commenced the three analyses to generate the parameters. In the first analysis, we generated a CBF map and CBV map by deconvolving the change in tissue concentration over the first pass of contrast agent with an arterial AIF using singular value decomposition (SVD) (Ostergaard *et al,* 1996*a, b*) (deconvolution method) and then calculating the mean transit time (MTT) by CBV/CBF. While this method generally yields accurate measurements of CBF, the flow estimates using SVD are susceptible to error due to bolus delay and dispersion. To improve reliability, we evaluated the PWI data by our second analysis, a pixel-based

numerical integration analysis with the measured data for calculation of the relative CBV (*rCBV*) and relative MTT (*rMTT*) (PIX method). The *rCBV* and *rMTT* were directly calculated from the time–ΔR_2 curve

$$rCBV = \int_{T_{start}}^{T_{end}} dt \cdot \Delta R_2(t) \quad (1)$$

$$rMTT = \frac{\int_{T_{start}}^{T_{end}} dt \cdot t\Delta R_2(t)}{\int_{T_{start}}^{T_{end}} dt \cdot \Delta R_2(t)} \quad (2)$$

where T_{start} was the starting time of the first pass of contrast medium in each pixel and T_{end} was the ending time. The relative CBF (rCBF) was obtained as *rCBV/rMTT*. Our third analysis was based on what we call the FIX method. The analysis was performed by measuring the mean start time and end time of the bolus passage of contrast medium in the entire brain and then applying the values to each pixel to measure parameters as the first-pass-start time and first-pass-end time, respectively. The equations to generate rCBV and rMTT were the same as those used in the PIX method. Having generally witnessed good correlations between FIX results and PET results in the past, we decided to include the former in this study. All the generated maps were filtered with a 5-mm full-width at half-maximum (FWHM) to achieve a resolution similar to that of the PET maps.

Positron Emission Tomography Study with ^{15}O Gases

The method used for our PET study has been described previously (Nariai *et al*, 1994). Briefly, the PET study was performed using a Headtome-V scanner (Shimadzu Corporation, Kyoto, Japan). The regional CBF and OEF were measured during continuous and consecutive 9-min inhalations of $C^{15}O_2$ and $^{15}O_2$ with continuous arterial blood sampling, employing a table-lookup technique (Senda *et al*, 1988). The regional CBF and OEF were obtained by calculating the values with lookup tables created from the arterial whole blood and plasma radioactivity curves, and then correcting them for delay and dispersion (Iida *et al*, 1986). The CBV was measured by a 3-min inhalation of $C^{15}O$ with blood sampling (Grubb *et al*, 1978). The OEF was corrected for the effect of the regional CBV (Lammertsma and Jones, 1983; Mintun *et al*, 1984). The MTT was calculated as *CBV/CBF*. All the PET images were reconstructed into a series of seven 5-mm-thick axial images with 7.5-mm intergaps, matched to the PWI level in each patient to set the regions of interests (ROIs) for PET and PWI in the same locations.

Analysis by Placing Region of Interests and Statistics

Abnormalities of cerebral hemodynamics in each patient were evaluated by manually placing the ROIs over the cerebral cortex (frontal, temporal parietal, and sensorimotor cortex) supplied by the internal carotid system (anterior circulation) and the upper cortex of the cerebellum, avoiding the infarcted area. Each ROI consisted of a series of 1-cm-diameter circles along the cortical rim. The mean values of MTT or rMTT, rCBF or CBF, and CBV or rCBV of the ROIs in each hemisphere were calculated (anterior MTT, anterior CBF, and anterior CBV, respectively) for both PWI and PET. In the PWI data, we also calculated the ratios of the anterior CBF (CBF ratio) and anterior CBV (CBV ratio) to the cerebellum. The corresponding data between the PWI and PET of CBF (PWI–CBF ratio versus PET–anterior CBF), CBV (PWI–CBV ratio versus PET–anterior CBV), and MTT (PWI–anterior MTT versus PET–anterior MTT) were compared with each other. The delay of the anterior MTT compared with the MTT or rMTT of the cerebellum measured by PWI was termed the 'MTT delay' and examined for correlations with the OEF and CBV obtained by PET.

All the data were expressed as mean ± s.d. Spearman's test and linear regression analysis were used to assess correlations between PWI and PET parameter values of the CBF ratio, CBV ratio, and anterior MTT. Correlations of the MTT delay of PWI with the OEF ratio and CBV from PET measurements were statistically analyzed by various regressions. Cluster analysis by the *K*-mean method was also applied to analyze the distribution of pixel values between PWI and PET. A *P*-value of <0.05 was considered statistically significant throughout the study.

Results

General Findings

Both PET and PWI data showed various hemodynamic abnormalities in unilateral or bilateral hemispheres in all of the patients studied. Yet, a comparison between the images obtained by the two methods clearly illustrated that only PWI could provide regional information on a gyrus-by-gyrus level (see Figure 1). Perfusion-weighted magnetic resonance imaging could be directly compared with morphological MRI, allowing the direct detection of abnormalities in CBF, CBV, and MTT on a precise anatomical basis. Perfusion-weighted magnetic resonance imaging could also be performed rapidly, with an acquisition time only 60 secs longer than that of a conventional MRI examination. Positron emission tomography, in contrast, took more time and required registration process with morphological images (Nariai *et al*, 1997; Shimada *et al*, 2000). The high spatial resolution of the MR perfusion maps was more useful for regional evaluation than the lower resolution of the PET images (Figure 1).

Correlation Between Magnetic Resonance Imaging and Positron Emission Tomography-Measured Cerebral Blood Flow, Cerebral Blood Volume, and Mean Transit Time

The correlations between PWI data and PET data on CBF, CBV, and MTT are illustrated in Figure 2. All CBV and MTT measurement variables calculated by the three analytic methods corresponded signifi-

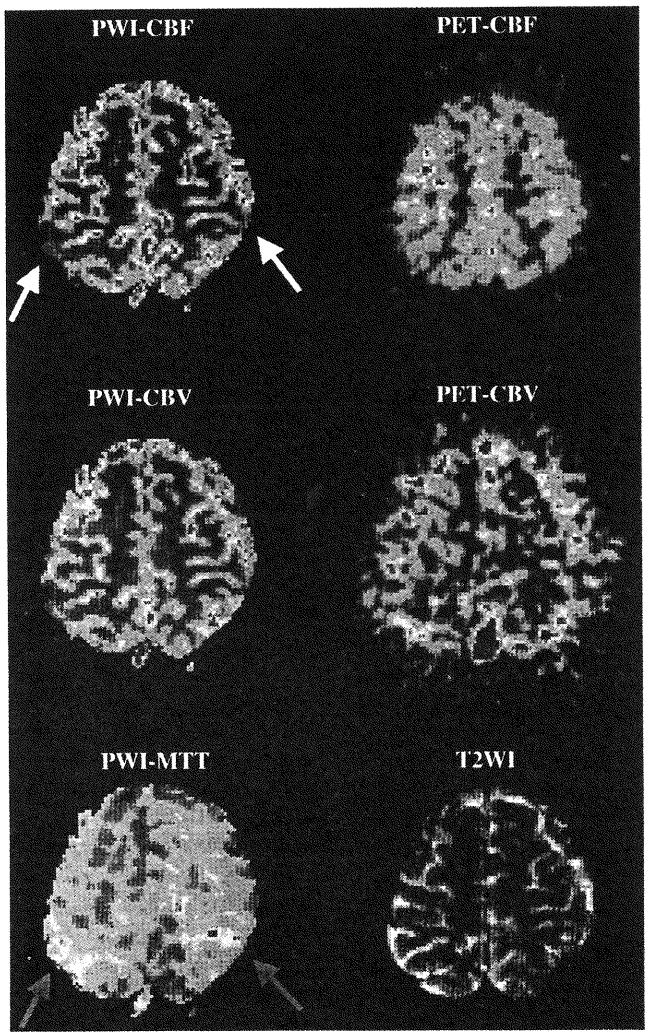

Figure 1 Parametric maps to indicate CBF and CBV obtained by PWI (Fix method) and PET in a 35-year-old woman with moyamoya disease. The MTT map of PWI is also shown. The CBF–PWI map indicated a decrease in CBF in the bilateral parietal regions (white arrows). The MTT-PWI map indicated MTT prolongation in the same regions (red arrows). The regional distribution of CBF and CBV detected by PWI correlated well with that detected by PET, but the spatial resolution of the former was far better than that of the latter.

cantly with the PET data. The CBV ratio obtained by the PIX method had the highest correlation with the PET-measured CBV value ($R^2 = 0.58$, $P < 0.01$, with the PIX method) among the three methods, and the ratios determined by the PIX and FIX analytic methods in the MTT measurement correlated well with the PET data ($R^2 = 0.58$, $P < 0.01$, with the PIX method; $R^2 = 0.67$, $P < 0.01$, with the FIX method). However, the only association between the PW1-measured CBF and PET-measured CBF was a weak but less than significant correlation determined by the FIX method ($R^2 = 0.06$, $P = 0.06$). Based on these results, variables applied by PIX and FIX methods were used for further analysis.

Detection of Misery Perfusion Using Perfusion-Weighted Magnetic Resonance Imaging

While the MTT has been used as an index of reduced cerebral perfusion pressure (Gibbs *et al*, 1984), an MTT prolonged beyond normal (i.e., reduced perfusion pressure) does not necessary lead to a reduced CBF. The compensatory mechanism to increase the focal vascular bed works well to preserve CBF until the reduction of perfusion pressure exceeds a certain threshold. This threshold is thought to correspond to the border between grade 1 and 2 hemodynamic stress, as defined by Powers *et al* (Powers, 1991; Powers *et al*, 1987). As MTT is theoretically considered a reciprocal of perfusion pressure, we might be able to detect grade 2 hemodynamic stress (misery perfusion) by defining the threshold of MTT prolongation.

In our comparison between PWI-MTT and PET-OEF on the parametric image maps, the areas with highly prolonged MTT closely corresponded with the areas with elevated OEF measured by PET (Figure 3). We therefore plotted the PET-measured OEF (ratio to control) against the MTT (MTT delay) measured by the PIX and FIX methods in the PWI analysis. Correlations between the MTT delay obtained by the PIX method and the OEF ratio obtained by PET were slightly better fit by quadratic correlation ($R^2 = 0.61$, $P < 0.001$) than by linear correlation ($R^2 = 0.57$, $P < 0.001$). Correlations between the MTT delay obtained by the FIX method and the OEF ratio obtained by PET were lower than that obtained by PIX method (quadratic correlation, $R^2 = 0.46$, $P < 0.001$; linear correlation, $R^2 = 0.43$, $P < 0.001$). Thus, the MTT delay calculated by the PIX method was used for further analysis (Figure 4). We statistically clustered the distribution of pixels into two categories by the *K*-mean method, as shown in the graph in Figure 4B. This figure clearly indicates the division of the pixels into normal OEF and abnormally elevated OEF using an MTT delay of 2.0 secs as a threshold. In the cerebral hemispheres where the MTT delay was within 2 secs, the OEF value did not exceed 120% of control. When the MTT delay exceeded 2 secs, however, the OEF value rose in proportion to the MTT delay. This suggests that the presence and grade of misery perfusion might be detectable by measuring the MTT delay with PWI.

In our examination of the relationship between the MTT delay by the PIX method and the CBV measured by PET, the latter tended to rise gradually in proportion to the duration of the MTT delay up to a delay of about 2.0 secs (Figure 4C). In the highly prolonged range, however, the CBV remained stably at around the 6 mL/100 g level irrespective of the duration of the MTT delay. The correlation between the MTT delay obtained by the PIX method on MRI and the CBV obtained by PET was slightly better fit by negative quadratic correlation ($R^2 = 0.34$, $P < 0.001$) than by linear correlation ($R^2 = 0.31$,

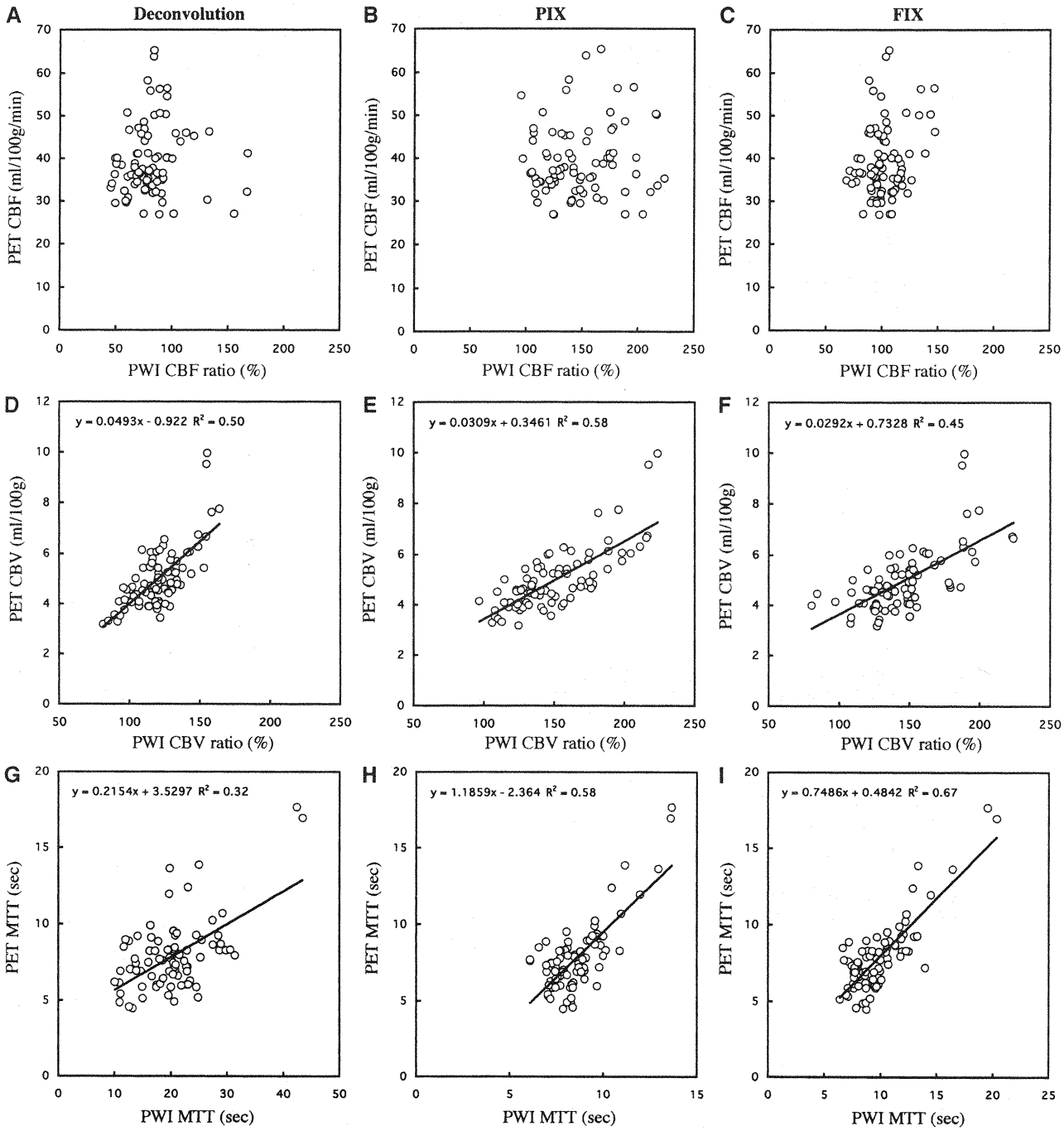

Figure 2 Correlation between PWI and PET measurements of CBF (**A–C**), CBV (**D–F**), and MTT (**G–I**). The correlation coefficient (R^2) obtained in each analysis is also displayed in each graph. All the CBV and MTT data generated by three methods were significantly correlated with CBV and MTT findings obtained by PET, respectively. There were no significant correlations between PWI and PET measurements of CBF (regression curve not shown).

$P<0.001$). By clustering the pixels into two categories, we could differentiate the dimension with prolonged MTT and elevated CBV from that with only moderate abnormalities of the two parameters (Figure 4D). Clustering on the *x*-axis was not as clearly depicted as it was in the case of OEF, but the MTT delay of 1.5 to 2.0 secs could be used as a divider.

Before applying the threshold MTT delay value in actual clinical decision-making, we need to ascertain its sensitivity and specificity in detecting abnormally elevated OEF and CBV using the 2-sec MTT delay as a threshold. We did this by calculating the sensitivity and specificity of the method in detecting the mean + 2s.d. of the OEF ratio to the cerebellum and CBV using normal control data from

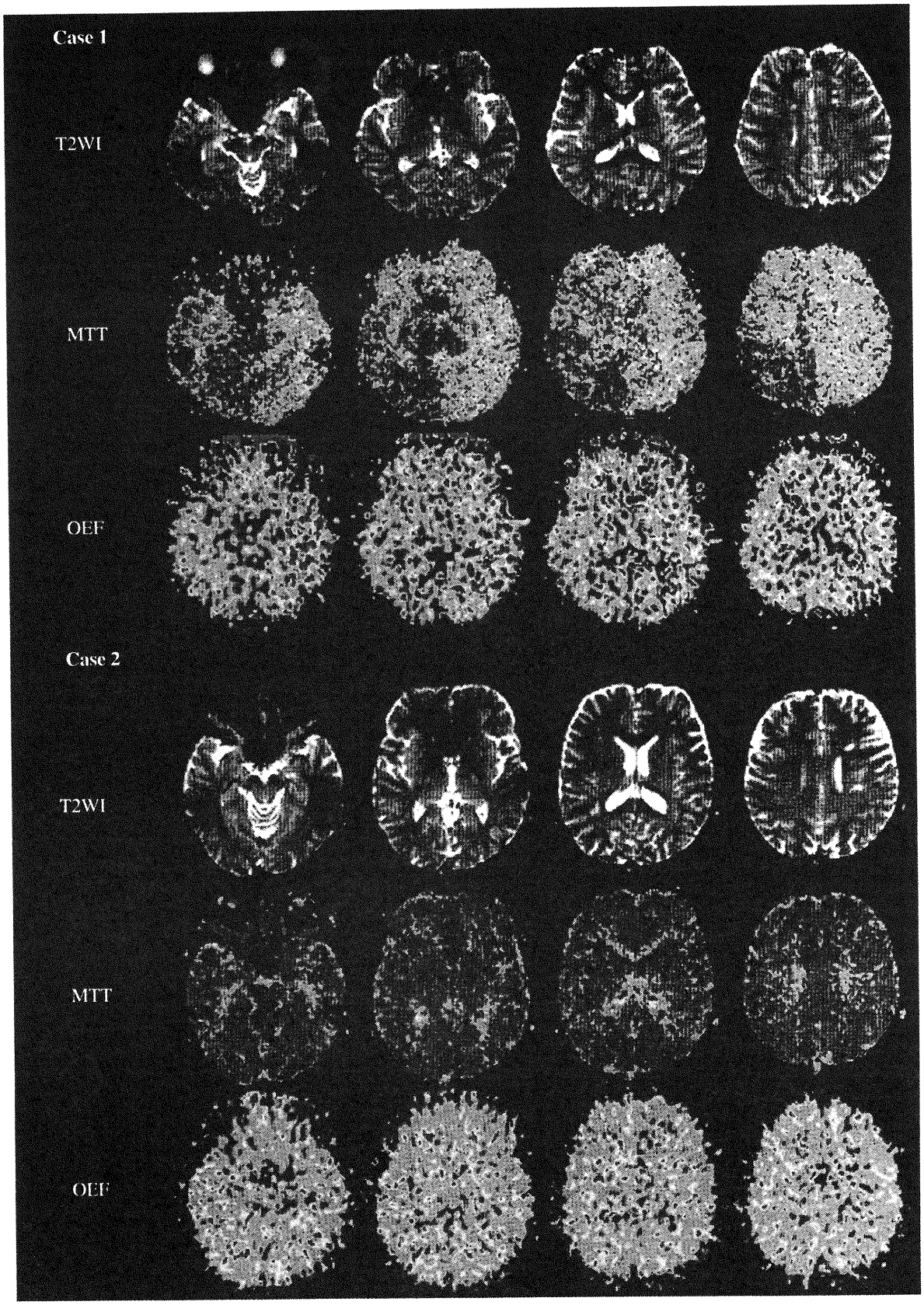
Case 1
T2WI
MTT
OEF
Case 2
T2WI
MTT
OEF

our earlier study (Nariai *et al*, 2005). Lines to indicate these threshold values are displayed in Figures 4B and 4D. Through the calculation with these values, we determined that the threshold MTT delay value of 2.0 secs had a sensitivity and specificity of 92.3% (12/13) and 100% (12/12) in detecting regions with abnormally elevated OEF ratio, and 20.0% (12/60) and 100% (12/12) in detecting regions with abnormally elevated CBV, respectively.

Discussion

In the present report, we used data from moyamoya patients to analyze whether the hemodynamic parameters obtained with PWI are reliable for use in clinical decision-making in the treatment of patients with chronic occlusive cerebrovascular disease.

In making clinical decisions in the treatment of patients with occlusive cerebrovascular disease, it is

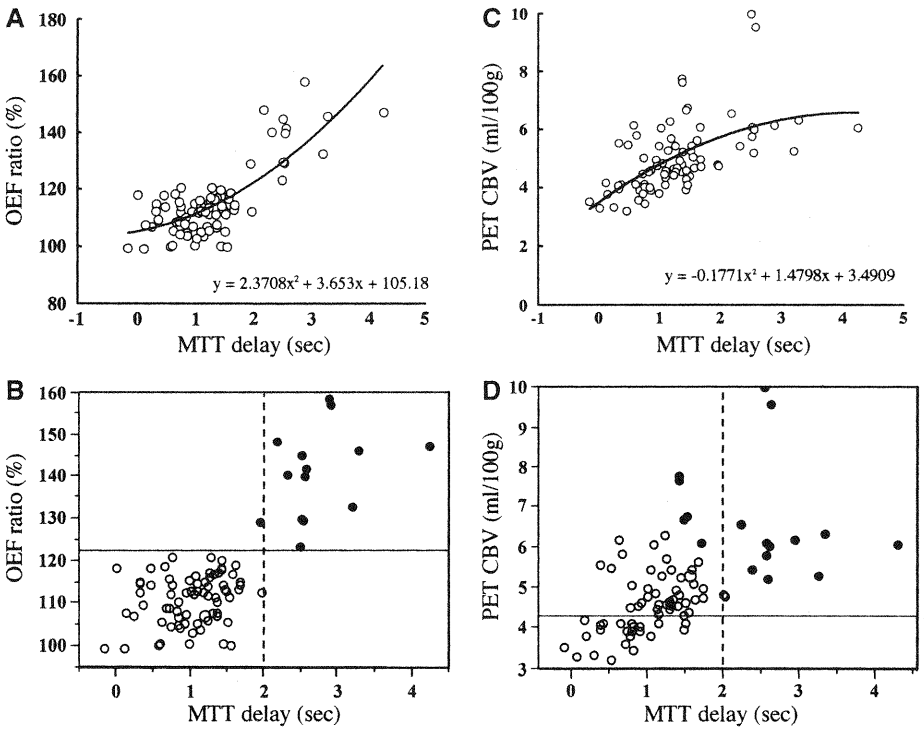

Figure 4 (**A**, **B**) show the correlation between the delay of PWI-MTT compared with the cerebellum (*x*-axis), and the PET-OEF ratio with the cerebellum (*y*-axis). The upper graph (**A**) shows the results of the regression analysis. The quadratic polynomial fits better than the linear polynomial, as indicated in the text. The lower graph (**B**) shows the results of cluster analysis by the *K*-mean method. The area with MTT delay of more than 2.0 secs shows an unmistakable elevation of OEF (indicated with black dots). The dotted vertical line indicates a 2.0-sec MTT delay and the horizontal solid line indicates the mean + 2s.d. of the OEF ratio among normal controls (121.7%). Using these values, the sensitivity and specificity in detecting the regions with abnormally elevated OEF ratios were calculated as 92.3% and 100%, respectively. (**C**, **D**) show the correlation between the delay of PWI-MTT compared with the cerebellum (*x*-axis) and PET-CBV (*y*-axis). The upper graph (**C**) shows the results of regression analysis. The quadratic polynomial fit better than the linear polynomial, as indicated in the text. The lower graph (**D**) shows the results of cluster analysis by the *K*-mean method. This graph indicates that the area with MTT delay of more than 2.0 secs comprised a group of regions with maximally elevated CBV (indicated with black dots). The dotted vertical line indicates a 2.0-sec MTT delay and the horizontal solid line indicates the mean + 2s.d. of CBV among normal controls (4.27). Using these values, the sensitivity and specificity in detecting the regions with abnormally elevated CBV were calculated as 20% and 100%, respectively. Perfusion-weighted imaging data was generated by the PIX method.

Figure 3 T2-weighted MRI (T2WI) (upper row), parametric maps to indicate MTT obtained with PWI (MTT) (middle row) and OEF images obtained with PET (lower row) of two representative moyamoya patients. Conventional MRI of case 1, a 26-year-old woman suffering from frequent temporary ischemic attacks (TIAs), depicted an infarcted area in the left frontal lobe. A parametric map of MTT showed a severe prolongation of transit time in the left entire hemisphere and right frontal lobe, and these findings closely corresponded with the OEF-elevated area. Case 2 was a 42-year-old woman who had been diagnosed with moyamoya disease incidentally and had no history of ischemic episodes. An infarcted area was also detected in the left frontal lobe, but the MTT map revealed almost normal circulation time in the entire brain. The parametric map of OEF also presented no abnormal elevation. MTT, mean transit time; OEF, oxygen extraction fraction; T2WI, echo-planar T2-weighted image.

now considered important to ascertain the degree of hemodynamic stress to predict the patient outcome (Derdeyn *et al,* 2002; Grubb *et al,* 1998). Simultaneous PET measurement of CBF and metabolism is the only known way to confirm the established risk factors (elevated OEF, misery perfusion, grade 2 hemodynamic stress). But rather than offering information of physiological significance, elevated OEF merely tells us that the decrease in focal perfusion pressure exceeds the maximum limit of the compensatory mechanism to increase the vascular bed for the preservation of CBF. As MTT measured by PWI is theoretically considered a reciprocal of perfusion pressure, we speculated that a comparison between PWI-measured MTT and PET-measured OEF may provide information useful for the detection of grade 2 hemodynamic stress.

In our analysis presented in Figure 4, OEF remained largely unchanged until the MTT delay in the anterior circulation of the cerebral hemisphere reached approximately 2 secs, whereupon it increased in proportion to the MTT delay beyond the 2-sec level. In our comparison of the CBV value from PET and the MTT value from the PIX method, however, the CBV showed no apparent increase once the MTT delay reached approximately 1.5–2.0 secs. The pixels were statistically clustered into two categories in both plots: pixels with only moderately prolonged MTT with normal OEF and moderately increased CBV, and pixels with markedly prolonged MTT with abnormally elevated OEF and saturated CBV.

By interpreting these plots with the theoretical consideration of the compensatory mechanism against major vessel occlusion proposed by Powers *et al* (Powers, 1991; Powers *et al,* 1987), we can align the threshold of the perfusion delay with the limit of vasodilatation to keep the CBF. In other words, we can detect the border between grade 1 and grade 2 hemodynamic stress at the threshold MTT delay value of around 2.0 secs, and the area with delay exceeding this point can be assumed to represent a state of misery perfusion. The analysis of sensitivity and specificity to detect abnormal OEF and CBV using this threshold value in Figure 4 also supports this assumption. High sensitivity and high specificity in detecting the region with elevated OEF indicate high reliability of the threshold MTT delay value to detect the border between grade 1 and grade 2. However, the low sensitivity of the 2.0-sec MTT delay in detecting the elevated CBV tells us that the CBV is already elevated before the MTT delay reaches 2.0 secs, without any corresponding elevation of OEF. This means, in turn, that the hemodynamic stress falls within the grade 1 range when the MTT delay remains less than 2.0 secs. Moreover, the 100% specificity of the more than 2 secs MTT delay in detecting elevated CBV tells us that grade 2 hemodynamic stress is always accompanied by elevated CBV. While several reports have investigated the use of PWI for the analysis of perfusion deficit (Baird and Warach, 1998; Maeda *et al,* 1999; Warach *et al,* 1996) and the loss of cerebrovascular reserve capacity (Schreiber *et al,* 1998) based on the MTT delay, no reports have interpreted the usefulness of the perfusion delay in depicting critical points for the prediction of misery perfusion. Our success in detecting this critical point by PWI in the present study may relate to the characteristics of moyamoya disease.

Moyamoya disease is a slowly progressive cerebrovascular disease which characteristically manifests variable degrees of perfusion deficit (Nariai *et al,* 2005). This variability in perfusion deficit makes the disease a suitable subject for comparative study using multiple modalities. However, our present results may also provide valuable insight into the specific pathophysiology of moyamoya disease. The application of PWI in cases with moyamoya disease has already been reported (Calamante *et al,* 2001; Kassner *et al,* 2003; Lee *et al,* 2003; Tsuchiya *et al,* 1998; Yamada *et al,* 1999). However, no studies have fully evaluated the accuracy of PWI measurement in moyamoya disease patients through comparisons with quantitative data acquired by other modalities, such as PET. Moyamoya disease usually exhibits a specific cerebral circulation pattern through leptomeningeal collaterals, and the focal perfusion is generally highly delayed. Thus, PWI and other methods to detect the bolus passage of contrast media are probably heavily affected by delay and dispersion (Calamante *et al,* 2000; Wu *et al,* 2003). Our result suggested that PWI potentially has the same level of reliability as PET in the quantitative measurement of CBV and MTT. Given the considerable scatter seen in the plots of Figure 2, however, caution should be taken in using this method for clinical decision-making. Henceforth, we will need to conduct ongoing comparative studies between PWI and PET to confirm the clinical reliability. Studies comparing the PWI parameters with clinical symptoms and treatment courses in individual patients with moyamoya disease will also be needed to confirm the utility of PWI measurement in the daily clinical setting.

In contrast to the PWI measurements of MTT and CBV and their promising utility, none of the three analysis methods using PWI showed any correlation with CBF measured by PET. We attributed this to the larger errors generated in the calculation of CBF due to the measurement errors of CBV and MTT in the PIX method. We also noted that the deconvolution method seemed to skew the CBF values. Further, the poor reliability of the AIF obtained from the internal carotid arteries already manifesting the lesional changes of the type seen in most patients with moyamoya disease hampers the accurate assessment of CBF by the AIF method.

Arterial spin-labeling (ASL) might have promise as an alternative method for evaluating CBF quantitatively. It should be noted, however, that ASL methods such as flow-sensitive alternating

inversion recovery (FAIR) can also be affected by the delay of the labeled spin passage (Calamante *et al*, 2001; Kim, 1995). Due to the specific circulation pattern of moyamoya disease, the transit time is prolonged and the FAIR technique is unable to differentiate between very long transit times and no flow (CBF = 0, no signal in the arterial spin labeling image).

As discussed above, our present analysis might be strongly influenced by the specific circulation pattern of moyamoya disease. To examine whether the same approach can be applied in other types of cerebrovascular disorder, we need to perform further comparative studies between PWI and PET with expanded populations of study candidates. Further research on the moyamoya patients from the present study is now underway to determine the correlations between the clinical features of the disease and the MTT delay measured in our current results. We are also currently conducting a prospective observation of both surgically and medically treated patients based on PWI data. These further analyses will better clarify the utility and limitations of PWI for clinical application.

In conclusion, PWI measurement provided sufficient quantitative evaluations of CBV and MTT in moyamoya patients. The measurement of CBF had limitations, however. Among the various parameters investigated, our results suggested that the duration of MTT delay might be used to detect the presence and degree of misery perfusion.

References

Baird AE, Warach S (1998) Magnetic resonance imaging of acute stroke. *J Cereb Blood Flow Metab* 18:583–609

Calamante F, Gadian DG, Connelly A (2000) Delay and dispersion effects in dynamic susceptibility contrast MRI: simulations using singular value decomposition. *Magn Reson Med* 44:466–73

Calamante F, Ganesan V, Kirkham FJ, Jan W, Chong WK, Gadian DG, Connelly A (2001) MR perfusion imaging in moyamoya syndrome: potential implications for clinical evaluation of occlusive cerebrovascular disease. *Stroke* 32:2810–6

Derdeyn CP, Videen TO, Yundt KD, Fritsch SM, Carpenter DA, Grubb RL, Powers WJ (2002) Variability of cerebral blood volume and oxygen extraction: stages of cerebral haemodynamic impairment revisited. *Brain* 125: 595–607

Gibbs JM, Leenders KL, Wise RJ, Jones T (1984) Evaluation of cerebral perfusion reserve in patients with carotid-artery occlusion. *Lancet* 1:182–6

Grubb RL, Jr, Derdeyn CP, Fritsch SM, Carpenter DA, Yundt KD, Videen TO, Spitznagel EL, Powers WJ (1998) Importance of hemodynamic factors in the prognosis of symptomatic carotid occlusion. *JAMA* 280:1055–60

Grubb RL, Jr, Raichle ME, Higgins CS, Eichling JO (1978) Measurement of regional cerebral blood volume by emission tomography. *Ann Neurol* 4:322–8

Iida H, Kanno I, Miura S, Murakami M, Takahashi K, Uemura K (1986) Error analysis of a quantitative cerebral blood flow measurement using H2(15)O autoradiography and positron emission tomography, with respect to the dispersion of the input function. *J Cereb Blood Flow Metab* 6:536–45

Ikezaki K, Matsushima T, Kuwabara Y, Suzuki SO, Nomura T, Fukui M (1994) Cerebral circulation and oxygen metabolism in childhood moyamoya disease: a perioperative positron emission tomography study. *J Neurosurg* 81:843–50

Kassner A, Zhu XP, Li KL, Jackson A (2003) Neoangiogenesis in association with moyamoya syndrome shown by estimation of relative recirculation based on dynamic contrast-enhanced MR images. *Am J Neuroradiol* 24:810–8

Kim SG (1995) Quantification of relative cerebral blood flow change by flow-sensitive alternating inversion recovery (FAIR) technique: application to functional mapping. *Magn Reson Med* 34:293–301

Lammertsma AA, Jones T (1983) Correction for the presence of intravascular oxygen-15 in the steady-state technique for measuring regional oxygen extraction ratio in the brain: 1. Description of the method. *J Cereb Blood Flow Metab* 3:416–24

Lee SK, Kim DI, Jeong EK, Kim SY, Kim SH, In YK, Kim DS, Choi JU (2003) Postoperative evaluation of moyamoya disease with perfusion-weighted MR imaging: initial experience. *Am J Neuroradiol* 24:741–7

Maeda M, Yuh WT, Ueda T, Maley JE, Crosby DL, Zhu MW, Magnotta VA (1999) Severe occlusive carotid artery disease: hemodynamic assessment by MR perfusion imaging in symptomatic patients. *Am J Neuroradiol* 20:43–51

Matsushima Y (1999) Moyamoya disease. In: *Principle and Practice of Pediatric Neurosurgery* (Albright A, Pollack I, Adelson P, eds), New York: Thieme, 1053–69

Mintun MA, Raichle ME, Martin WR, Herscovitch P (1984) Brain oxygen utilization measured with O-15 radiotracers and positron emission tomography. *J Nucl Med* 25:177–87

Nariai T, Matsushima Y, Imae S, Tanaka Y, Ishii K, Senda M, Ohno K (2005) Severe hemodynamic stress in selected subtypes of patients with moyamoya disease—a positron emission tomography study. *J Neurol Neurosurg Psychiatry* 76:663–9

Nariai T, Senda M, Ishii K, Maehara T, Wakabayashi S, Toyama H, Ishiwata K, Hirakawa K (1997) Three-dimensional imaging of cortical structure, function and glioma for tumor resection. *J Nucl Med* 38:1563–8

Nariai T, Suzuki R, Hirakawa K, Maehara T, Ishii K, Senda M (1995) Vascular reserve in chronic cerebral ischemia measured by the acetazolamide challenge test: comparison with positron emission tomography. *Am J Neuroradiol* 16:563–70

Nariai T, Suzuki R, Matsushima Y, Ichimura K, Hirakawa K, Ishii K, Senda M (1994) Surgically induced angiogenesis to compensate for hemodynamic cerebral ischemia. *Stroke* 25:1014–21

Ostergaard L, Johannsen P, Host-Poulsen P, Vestergaard-Poulsen P, Asboe H, Gee AD, Hansen SB, Cold GE, Gjedde A, Gyldensted C (1998*a*) Cerebral blood flow measurements by magnetic resonance imaging bolus tracking: comparison with [(15)O]H_2O positron emission tomography in humans. *J Cereb Blood Flow Metab* 18:935–40

Ostergaard L, Smith DF, Vestergaard-Poulsen P, Hansen SB, Gee AD, Gjedde A, Gyldensted C (1998*b*) Absolute cerebral blood flow and blood volume measured by